



This article was originally published in a journal published by Elsevier, and the attached copy is provided by Elsevier for the author's benefit and for the benefit of the author's institution, for non-commercial research and educational use including without limitation use in instruction at your institution, sending it to specific colleagues that you know, and providing a copy to your institution's administrator.

All other uses, reproduction and distribution, including without limitation commercial reprints, selling or licensing copies or access, or posting on open internet sites, your personal or institution's website or repository, are prohibited. For exceptions, permission may be sought for such use through Elsevier's permissions site at:

<http://www.elsevier.com/locate/permissionusematerial>

# Viscoplastic flow over an inclined surface<sup>☆</sup>

Neil J. Balmforth<sup>a,c,\*</sup>, Richard V. Craster<sup>b</sup>, Alison C. Rust<sup>c</sup>, Roberto Sassi<sup>d,1</sup>

<sup>a</sup> Department of Mathematics, University of British Columbia, Vancouver, Canada

<sup>b</sup> Department of Mathematics, Imperial College London SW7 2AZ, UK

<sup>c</sup> Department of Earth and Ocean Science, University of British Columbia, Vancouver, Canada

<sup>d</sup> Dipartimento di Tecnologie dell'Informazione, Università di Milano, Crema, Italy

Received 15 March 2006; received in revised form 10 July 2006; accepted 13 July 2006

## Abstract

We review viscoplastic flow over inclined surfaces, focusing on constant-flux extrusions from small vents and the slumping of a fixed volume of material. Lubrication theory is used for shallow and slow flows to reduce the governing equations to a nonlinear diffusion-type equation for the local fluid depth; this model is used as the basis for exploration of the problem. Theory is compared to experiments. A number of complications and additional physical effects are discussed that enrich real situations.

© 2006 Elsevier B.V. All rights reserved.

**Keywords:** Viscoplastic fluids; Similarity solutions; Yield stress

## 1. Introduction

As reviewed by Ancy in this volume [1] a large number of problems in geophysics and engineering surround the flow of a viscoplastic fluid over an inclined surface. Our goal in the current article is to consider the problem as a basic type of fluid dynamical flow, review some of the efforts to model the situation and highlight the current status of the subject. We focus on viscoplastic fluids that have a well-defined yield stress in combination with power-law viscous behaviour (*i.e.* Herschel–Bulkley fluids). However, we also review some of the many complications introduced by a range of other physical effects, which enrich the dynamics of real flows.

Of course, even flow of a Newtonian fluid over a surface is not straightforward and is still a subject of active research. Making the fluid non-Newtonian only adds to the richness, so we must make some idealizations and simplifications to gain some inroads into the problem. The main simplification we make here is that the fluid is relatively shallow and flows slowly. Thus, we take advantage of a lubrication-style approximation to the

governing fluid equations to reduce them into a single evolution equation for the local fluid depth. This trick is well used in a great many fluid problems (ranging from engineering tribology to glaciology), and can similarly be used to great effect for viscoplastics.

To be more specific, we use the lubrication model to explore two canonical examples that illustrate some of the distinctive features of how viscoplastic fluid flows over inclined surfaces and highlight the main differences with the equivalent Newtonian problem:

- The growth of an inclined fluid structure by extrusion from a small vent.
- The slump to rest of a suddenly released, fixed mass of fluid.

Extrusions and slumps are a component of a large number of industrial processes and occur in various geological problems (such as mudslides and lava flows) [2,3,8,9,4–6].

The key differences between viscoplastic and Newtonian film flow come about chiefly because of the yield stress, which can hold the fluid rigid even when acted upon by external forces and internal stresses. Consequently, plugs and stagnant zones form adjoining regions of true deformation and flow. Indeed, a gross idealization might say that viscoplastic flow dynamics is all about the interplay of plug regions and yield zones. This defines a complicated free boundary problem that to date has resisted much analysis. At the birth of the subject, attacks on the prob-

<sup>☆</sup> Part of this work was presented at the BIRS workshop: “Viscoplastic fluids: from Theory to Application”, Banff (AB), CA, October 22–27, 2005.

\* Corresponding author.

E-mail address: [njb@math.ubc.ca](mailto:njb@math.ubc.ca) (N.J. Balmforth).

<sup>1</sup> This author was partially supported by EPSRC through Grant number GR/S47663/01.

lems were limited, including only some exact solutions suited to very simple flow geometries (such as standard solutions like Poiseuille flow and Oldroyd's use of the hodograph technique [10]). More recently, with the use of clever numerical methods and asymptotics, the subject has significantly advanced; other papers in the current volume mention the latest attempts to deal with some of the outstanding issues. Our focus here is on using asymptotic methods for shallow flows.

One key feature of viscoplastic flow dynamics that comes out naturally in the shallow limit is the notion of a “pseudo-plug” [11]: a region that is neither completely rigid, nor freely shearing. The material inside the pseudo-plug is very weakly yielded and acts much like a perfectly plastic material. The viscoplastic fluid dynamics thus shares many common aspects with conventional plasticity theory. Pseudo-plugs dominate the dynamics over substantial regions of shallow flows and arise naturally when there is a separation of length scales.

The use of lubrication approximation in thin films dates back to Reynolds [12]. For Newtonian films with free surfaces, flow over inclined planes was discussed by Huppert [13] and Lister [16]. Simple extensions have also been made to power-law fluids, which have notable application in glaciology (the “shallow-ice approximation”; e.g. [17]). For viscoplastic fluids, Liu and Mei [18,19] presented the lubrication model for two-dimensional (sheet) flow and applied it to problems of mud flow (see also [20–22]). Balmforth et al. [5] considered the axisymmetric version of the problem and, following earlier work by Hulme [2], Blake [3] and Griffiths and Fink [6], modelled the extrusion of lava domes. Most recently, the lubrication model has been extended to three dimensions [23–25]. There are also applications to flows over varying topographies [35,59] and around cylinders [60]. A tangential vein of literature generalizes the Newtonian self-similar solution of Smith [62] to the problem of a steady, gradually widening flow of a viscoplastic “rivulet” down an inclined plane [27,61].

From the rheological viewpoint, flow over flat or inclined planes offers a straightforward vision of a relatively simple dynamics, which suggests that observations could provide insight into material behaviour. Indeed, two flows in particular have been suggested in the past as means to determine yield stress: the initiation or cessation of flow of a film on an

inclined plane as one varies the slope was suggested by De Kee et al. [26], much as one measures the friction angles of a granular material. Second, the “slump test” was advocated by Pashias et al. [7] as a “fifty cent rheometer”. Here, one measures the final shape of a slumped dome of material of given volume. Coussot et al. [9] suggested the same methodology for slumps on inclined surfaces. A key difference between the mudflows of Mei et al. and the typical slump test of materials like concrete is that whereas the former is often a shallow flow, the latter can be quite the opposite. As a result, the modelling of slump tests has proceeded in somewhat different directions than we take here [28]. Unfortunately, without the simplifications of lubrication theory, the problem is much more complicated and far less can be gleaned about the general flow dynamics.

## 2. Mathematical formulation

### 2.1. The flow of a two-dimensional sheet on an inclined plane

We begin with the governing equations for a two-dimensional, incompressible fluid on an inclined plane. As illustrated in Fig. 1, we align coordinates so that the plane occupies  $z=0$ , and  $x$  points downslope. The fluid velocity field is  $(u(x, z, t), w(x, z, t))$  and  $p(x, z, t)$  is the pressure. Conservation of mass and momentum then read:

$$u_x + w_z = 0, \quad (1)$$

$$\rho(u_t + uu_x + ww_z) = -p_x + \partial_x \tau_{xx} + \partial_z \tau_{xz} + \rho g \sin \phi, \quad (2)$$

and

$$\rho(w_t + uw_x + ww_z) = -p_z + \partial_x \tau_{xz} + \partial_z \tau_{zz} - \rho g \cos \phi, \quad (3)$$

where  $\rho$  is the density,  $g$  the gravity,  $\phi$  is the angle of the inclined plane, and subscripts denote partial derivatives except for the deviatoric stress components,  $(\tau_{xx}, \tau_{xz}, \tau_{zz})$ .

The Herschel–Bulkley law is formulated mathematically as follows:

$$u_x = w_z = u_z + w_x = 0, \quad \text{for } \tau \equiv \sqrt{\tau_{xx}^2 + \tau_{xz}^2} < \tau_y, \quad (4)$$

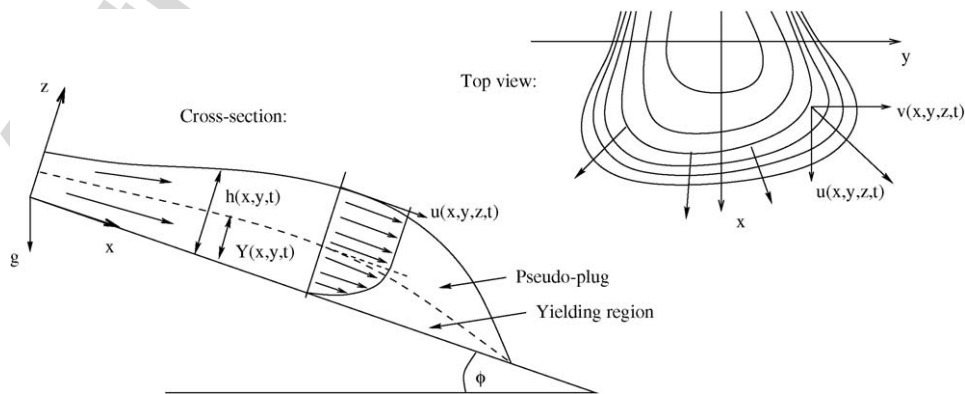


Fig. 1. Sketch of a flow on an inclined plane.  $\phi$  is the angle of inclination to the horizontal.

$$\begin{pmatrix} \tau_{xx} & \tau_{xz} \\ \tau_{xz} & \tau_{zz} \end{pmatrix} = \frac{1}{\dot{\gamma}} (K\dot{\gamma}^n + \tau_y) \begin{pmatrix} 2u_x & u_z + w_x \\ u_z + w_x & 2w_z \end{pmatrix},$$

for  $\tau \geq \tau_y$ ,

where

$$\dot{\gamma} \equiv \sqrt{(u_z + w_x)^2 + 4u_x^2}.$$

The model has three parameters, assumed constant:  $K$  (the consistency),  $\tau_y$  (the yield stress) and  $n$  (the power-law index).

We impose no slip on the inclined plane, so that  $u = w = 0$  on  $z = 0$ . The upper surface,  $z = h(x, t)$ , is a material surface and stress free. The latter conditions, assuming atmospheric pressure to be a negligible constant and ignoring surface tension, can be formulated by taking the product of the normal vector to the surface with the stress tensor. After a little algebra, the surface boundary conditions can be summarized as:

$$\left. \begin{aligned} h_t + uh_x &= w \\ (1 - h_x^2)p + (1 + h_x^2)\tau_{xx} &= 0 \\ (1 - h_x^2)\tau_{xz} - 2h_x\tau_{xx} &= 0 \end{aligned} \right\} \text{ on } z = h(x, t). \quad (6)$$

## 2.2. Non-dimensionalization and the lubrication model

To remove dimensions we use the typical film thickness ( $H$ ), to measure lengths transverse to the film (which we loosely refer to as “vertical”), and  $L$  for distances downslope (loosely called “horizontal”); the aspect ratio,  $\varepsilon = H/L$  is a key, small parameter. We then set

$$\begin{aligned} x &= L\tilde{x}, \quad z = H\tilde{z}, \quad u = V\tilde{u}, \quad w = \frac{HV\tilde{w}}{L}, \quad t = \frac{L\tilde{t}}{V}, \\ h &= H\tilde{h}, \quad p = \rho g H \tilde{p} \cos \phi, \quad \dot{\gamma} = \frac{V}{H} \tilde{\gamma}, \quad \tau_{jk} = \rho v \frac{V}{H} \tilde{\tau}_{jk}, \end{aligned} \quad (7)$$

and so on, where  $V = gH^3 \cos \phi / (\nu L)$  is a characteristic flow speed, and  $\nu = K(V/H)^{n-1} / \rho$  is an effective kinematic viscosity. After dropping the tilde decoration, the dimensionless equations become:

$$u_x + w_z = 0, \quad (8)$$

$$\varepsilon Re(u_t + uu_x + ww_z) = -p_x + \varepsilon \partial_x \tau_{xx} + \partial_z \tau_{xz} + S, \quad (9)$$

$$\varepsilon^3 Re(w_t + uw_x + ww_z) = -p_z + \varepsilon^2 \partial_x \tau_{xz} + \varepsilon \partial_z \tau_{zz} - 1, \quad (10)$$

$$\begin{pmatrix} \tau_{xx} & \tau_{xz} \\ \tau_{xz} & \tau_{zz} \end{pmatrix} = \frac{1}{\dot{\gamma}} (\dot{\gamma}^n + B) \begin{pmatrix} 2\varepsilon u_x & u_z + \varepsilon^2 w_x \\ u_z + w_x & 2\varepsilon w_z \end{pmatrix},$$

for  $\tau \geq B$ ,

and

$$\dot{\gamma} = u_x = w_z = u_z + w_x = 0, \quad \text{for } \tau < B, \quad (12)$$

where  $S = \varepsilon^{-1} \tan \phi$  is a slope parameter that can be set to unity unless the plane is horizontal, and two important dimensionless

groups appear,

$$Re = \frac{VH^2}{\nu L} \quad \text{and} \quad B = \frac{\tau_y H}{\rho \nu V},$$

which are the Reynolds number based on the characteristic speed  $V$ , and the Bingham number (dimensionless yield stress).

Our slow and shallow flow approximation amounts to taking  $\varepsilon \ll 1$  and keeping  $Re$  order one. One can then drop all terms of order  $\varepsilon$  or higher from the momentum equations which then simply express the dominant force balance. The equations can be integrated in  $z$ , to find

$$p = h - z \quad \text{and} \quad \tau_{xz} = (S - h_x)(h - z), \quad (13)$$

which uses the leading-order stress-free boundary conditions,  $p = \tau_{xz} = 0$  on  $z = h$ . With these quantities in hand, we may find the velocity components from the constitutive law and continuity. For example,

$$\begin{aligned} u &= \frac{n|S - h_x|^{1/n}}{n+1} \text{sgn}(S - h_x) \\ &\times \begin{cases} [Y^{1+1/n} - (Y - z)^{1+1/n}], & z \leq Y \\ Y^{1+1/n}, & z > Y \end{cases}, \end{aligned} \quad (14)$$

where

$$Y = \max \left( h - \frac{B}{|S - h_x|}, 0 \right), \quad (15)$$

which is illustrated in the sketch of Fig. 1. The surface,  $z = Y(x, t)$ , separates a shearing flow adjacent to the plane from a plug-like superficial flow. It is not a true plug because the material actually lies order  $\varepsilon$  above the yield stress for  $z > Y(x, t)$ , which circumvents some inconsistencies that would otherwise seem to occur within the lubrication theory [29,23]. The weak yielding allows the material in the “pseudo-plug” to spread and flow over the plane.

Finally, the application of the kinematic surface boundary condition leads to the evolution equation,

$$\begin{aligned} h_t + \partial_x \left[ \frac{nY^{1+(1/n)} |S - h_x|^{(1/n)-1}}{(1+n)(1+2n)} (2nh + h - nY)(S - h_x) \right] \\ = w_s(x, t), \end{aligned} \quad (16)$$

where  $w_s(x, t)$  is a prescribed function that represents any source of fluid on the plane, such as a localized vent.

## 2.3. Three-dimensional lubrication flow

In three dimensions, we add the cross-slope coordinate,  $y$ , and velocity  $v(x, y, z, t)$ . The scaling and lubrication theory follow much as above. We quote only the final formula for the evolution equation for  $h(x, y, t)$ :

$$\begin{aligned} h_t + \mathcal{U}_x + \mathcal{V}_y &= w_s(x, y, t), \\ \left( \frac{\mathcal{U}}{\mathcal{V}} \right) &= \frac{nY(sY)^{1/n} [(1+2n)h - nY]}{s(n+1)(2n+1)} \begin{pmatrix} S - h_x \\ -h_y \end{pmatrix}, \end{aligned}$$

where

$$Y(x, y, t) = \max \left( h - \frac{B}{s}, 0 \right) \quad \text{and} \quad s = \sqrt{(S - h_x)^2 + h_y^2},$$

the depth-integrated velocity field is  $(\mathcal{U}, \mathcal{V})$ , and  $s$  is the slope of the fluid surface.

For Bingham fluids, the evolution equation simplifies to

$$h_t + \mathcal{U}_x + \mathcal{V}_y = w_s, \quad \begin{pmatrix} \mathcal{U} \\ \mathcal{V} \end{pmatrix} = \frac{1}{6} Y^2 (3h - Y) \begin{pmatrix} S - h_x \\ -h_x \end{pmatrix}, \quad (17)$$

We consider this model for most of our examples. In general situations, the equations must be solved numerically; we use the scheme discussed in [Appendix A](#).

### 3. Limiting dynamics

Before considering our two model problems, we briefly digress to describe some features of the lubrication theory, which serve to illustrate the dynamics it captures and help prepare for some of the analysis to come.

#### 3.1. Yielding and cessation conditions; planar slumps

The condition for yield in the full Herschel–Bulkley law corresponds to the von Mises yield criterion, which is commonly used in plasticity theory (*e.g.* [30]), but is complicated to deal with in most situations. By contrast, in the lubrication model, this condition is particularly simple: when  $Y \rightarrow 0$ , the shearing region at the base of the fluid layer vanishes and the pseudo-plug fills the entire fluid depth, at which point it becomes a real rigid plug. The yield condition is the same whether it marks the initiation or cessation of flow and can be written in the form,

$$h \geq \frac{B}{s}, \quad \text{or} \quad (S - h_x)^2 + h_y^2 \geq \frac{B^2}{h^2}. \quad (18)$$

If these conditions are violated, the fluid layer is insufficiently stressed to flow.

The equality in (18) describes the final resting state of those parts of the fluid layer that yielded during its evolution, if the ultimate fate of the fluid is to come to a standstill. That is, the limiting state wherein the stresses over the yielded regions decline and approach the yield stress from above. We give a fuller discussion of such states in [Section 5](#) when we examine the final shape of slumps, describing how they may be constructed analytically using Charpit's method. Even when the fluid does not come to rest, but flows continually, the solution of the limiting problem,  $Y \rightarrow 0$ , can still be relevant. For example, the limit also characterizes slow, yield-stress dominated flows like the extrusions of [Section 4](#) with  $B \gg 1$ .

For a two-dimensional sheet of fluid, the limiting state is described by the even simpler relation,

$$h|S - h_x| = B, \quad (19)$$

which can be straightforwardly integrated to give an implicit solution for the profile:

$$h(x) - h(X) \pm \frac{B}{S} \log \left[ \frac{B \mp Sh(x)}{B \mp Sh(X)} \right] = x - X, \quad (20)$$

where the constant of integration has been fixed by assuming that we know  $h(x)$  at  $x = X$ . Which of the two branches of the solution one takes depends on whether the background inclination opposes or compounds the tilt of the fluid surface.

By way of illustration, we display in [Fig. 2](#) numerical solutions showing the slump of a two-dimensional block of Bingham fluid over an inclined surface. Three cases are shown with different Bingham numbers. In the first panel, the collapse of the block's walls forces fluid to yield within localized strips adjacent to the edges. However, the central areas of the fluid are held in place by the yield stress throughout the slump. Flow eventually ceases when the surface slopes decline sufficiently, leading to a final deposit with a central, stagnant core, buffered by the profiles (20). In the second case, the central core is again held in place during the initial collapse of the block's walls. Now, however, the yielding regions widen until they meet near  $x = -0.3$ , by which point the entire fluid layer has yielded. The flow again comes to rest; this time the final shape is given by the two branches of the profile (20), pieced together at the common apex of the slumped structure. The apex has a discontinuity in surface slope, and roughly marks the division between fluid slumping in either direction. In the final example, the yield stress is too small even to hold the central core in place ( $h(x, 0) = 1 > B/S$ ), and the whole block yields immediately. The final shape is another, fully slumped structure given by (20).

The three-fold characterization of the slumps illustrated in [Fig. 2](#) carries over to more general situations, such as three-dimensional dam breaks ([Section 5](#)). The first two examples illustrate “edge collapses”, in which only the walls of the initial structures suffer mechanical failure; they differ in the later stages of the slump when it transpires whether or not part of the initial shape is left intact. The background slope is not essential here, and both kinds of edge collapse occur over flat surfaces. The third case is a “layer collapse”, much like a landslide, and can only occur when there is a relatively strong background slope. For flat-topped initial states with unit depth, which kind of slump occurs depends on  $B$  and the initial width. But in all three cases, we observe flows that decelerate to rest, leaving states marked with points of surface-slope discontinuity.

More solutions of the one-dimensional problem are presented in various other articles: Liu and Mei [18] consider a range of kinematic-wave-type solutions, and one-dimensional extrusions (*i.e.* line sources) are explored by Balmforth et al. [24]. Slumps specifically with the form of dam breaks are given by Matson and Hogg [31] and Balmforth et al. [32] in this volume. One notable feature of these dam break solutions, and also the slumps shown in [Fig. 2](#), is that the approach to the final state is relatively slow (with dependence  $1/t$ ), which can be verified either numerically or asymptotically.

Note that [Eq. \(19\)](#) can be derived more directly from the original governing equations by noticing that they follow from



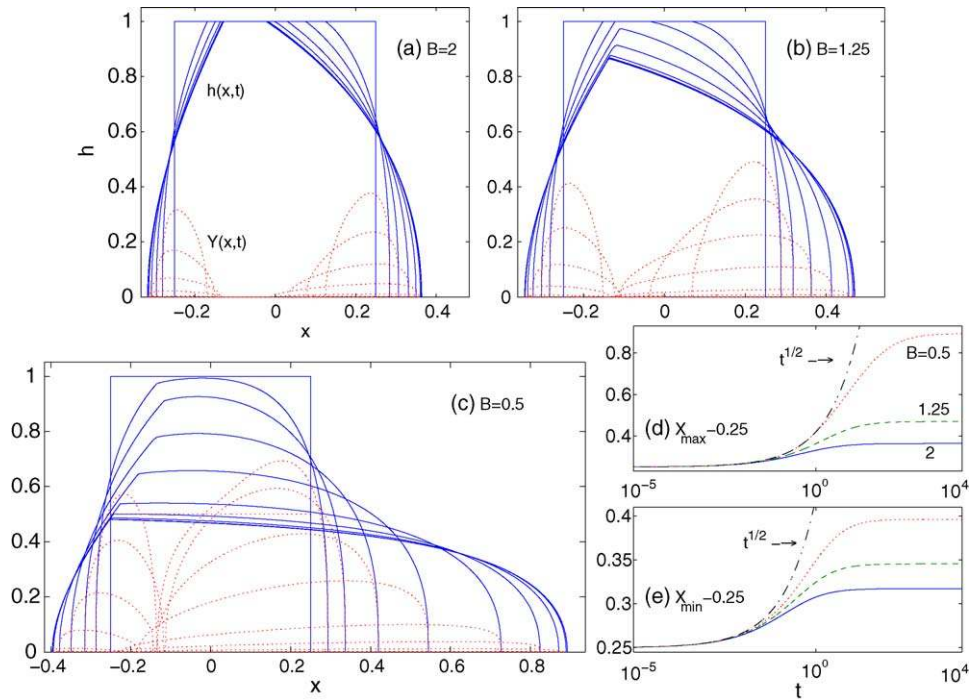


Fig. 2. Numerical solutions showing the slump of a two-dimensional block of fluid on an incline. Snapshots of  $h$  (solid lines) and  $Y$  (dotted lines) are shown for (a)  $B=2$ , (b)  $B=1.25$  and (c)  $B=0.5$  (the snapshots are at  $t=0, 0.0625, 0.25, 1, 4, 100, 400, 2500, 10^4$ ). In panels (d) and (e), we show time series of the downstream and upstream fluid edges,  $X_{\max}$  and  $X_{\min}$ , respectively. Also indicated is a  $\sqrt{t}$  dependence that fits the early part of the data.

asymptotic approximation of the plasticity problem:

$$\varepsilon \partial_x \tau_{xx} + \partial_z \tau_{xz} = p_x - S, \quad (21)$$

$$\varepsilon^2 \partial_x \tau_{xz} + \varepsilon \partial_z \tau_{zz} = p_z + 1, \quad (22)$$

$$\tau_{xz}^2 + \tau_{xx}^2 = B^2, \quad (23)$$

with the usual stress-free surface boundary conditions, supplemented by the basal condition,  $\tau_{xx} = 0$ , which corresponds to the existence of a boundary layer of thin, sheared fluid adjacent to the plane. We mention the latter point primarily to indicate how one might construct the final state of a non-shallow fluid layer with  $\varepsilon \sim O(1)$  (see later).

### 3.2. Large slope

Although the lubrication problem in (17) is not analytically tractable in general, one limit that does heed to further analysis is that of “large” slope,  $S$ . At first sight, this limit sounds a little curious since we have already claimed that one can scale  $S$  to unity, provided the plane is not horizontal. In fact, the whole lubrication analysis is laid out assuming that  $S = (L/H)\tan\phi$  is an order one parameter, which demands relatively mild slopes. However, one can also consider order-one slopes provided one revises the asymptotic scalings and scheme. The result is the three-dimensional evolution equation,

$$h_t + \frac{1}{6}[(h-B)^2(2h+B)]_x = 0, \quad \text{if } h > B, \quad (24)$$

and  $h_t = 0$  otherwise. This evolution equation is nothing more than our standard lubrication model with  $|h_x, h_y| \ll S$ , and is

really what is meant by “large slope  $S$ ”. The equivalent approximation of the Newtonian problem is considered by Lister [16]; Huang and Garcia [22] and Ancey [1] also present versions of [24].

Eq. (24) is easily solved using the usual method of characteristics for quasi-linear partial differential equations. Indeed, it is a standard shock-forming equation and to determine the solution, one suitably translates the initial profile downslope. If  $h_I(x_0, y) = h(x_0, y, 0)$ , then implicitly we have

$$h(x, y, t) = h_I(x_0, y),$$

$$x = x_0 + th_I(x_0, y)\max[h_I(x_0, y) - B, 0]. \quad (25)$$

The main novelty in the solution lies in the yield condition: only that part of the solution with  $h > B$  moves downslope. For those parts of the fluid layer, the thicker regions travel fastest, and so the top of the profile overtakes the shallower and static parts ahead leading to a multivalued solution. As in a great many other hyperbolic problems, one needs to regularize this behaviour by inserting a shock. As used in [14,15] for a Newtonian fluid, a Maxwell-(equal area)-type construction can be used to insert the shock so that the solution is single valued (if discontinuous) and conserves mass.

The shock speed follows from returning to the full equation and performing a boundary layer expansion. Even without solving for the shock path in detail, we can predict the final state: as time goes on the multivalued solution becomes increasingly displaced downstream. However, it has limited area and so becomes a long skinny finger. The equal area rule demands that the shock is placed in the solution close to the downslope edge of the yielded region. Thus, to calculate the final state, we take

the initial profile and truncate it at  $h=B$  to form a “pedestal”; we then extend the pedestal downstream by adding the material that is cut away, keeping the level at  $h=B$ , and cutting it off abruptly at a stationary shock such that mass is conserved. In two dimensions, one does this for the whole profile at once; in three dimensions, for each section in  $y$  separately. In practice one could even improve the final profile by inserting the  $Y \rightarrow 0$  analytical solution.

Fig. 3 presents an illustration of the characteristics solution and the insertion of the shock. Here, a slumping Gaussian mound is shown in both two and three dimensions. The characteristics solution is also compared with numerical computations of the thin-layer equation. All in all, we see that slumps on steep slopes develop wide plateaux with almost vertical cliffs at their downstream edges.

#### 4. Extrusions

In this section, we consider extrusions from a localized, circular source. Our exploration is based in part on the study of Balmforth, Craster & Sassi [24], who describe extrusions of this kind, as well as flows from fixed apertures. As a model for the source, we fix

$$w_s = W(t) \begin{cases} 3\pi^{-1}r_*^{-2} \left(1 - \frac{r^2}{r_*^2}\right)^2, & r = \sqrt{x^2 + y^2} \leq r_* \\ 0, & r = \sqrt{x^2 + y^2} > r_* \end{cases} \quad (26)$$

where  $r_*$  is the vent radius, and  $W(t)$  describes the amplitude and variability of total the source flux. Once the extruded fluid

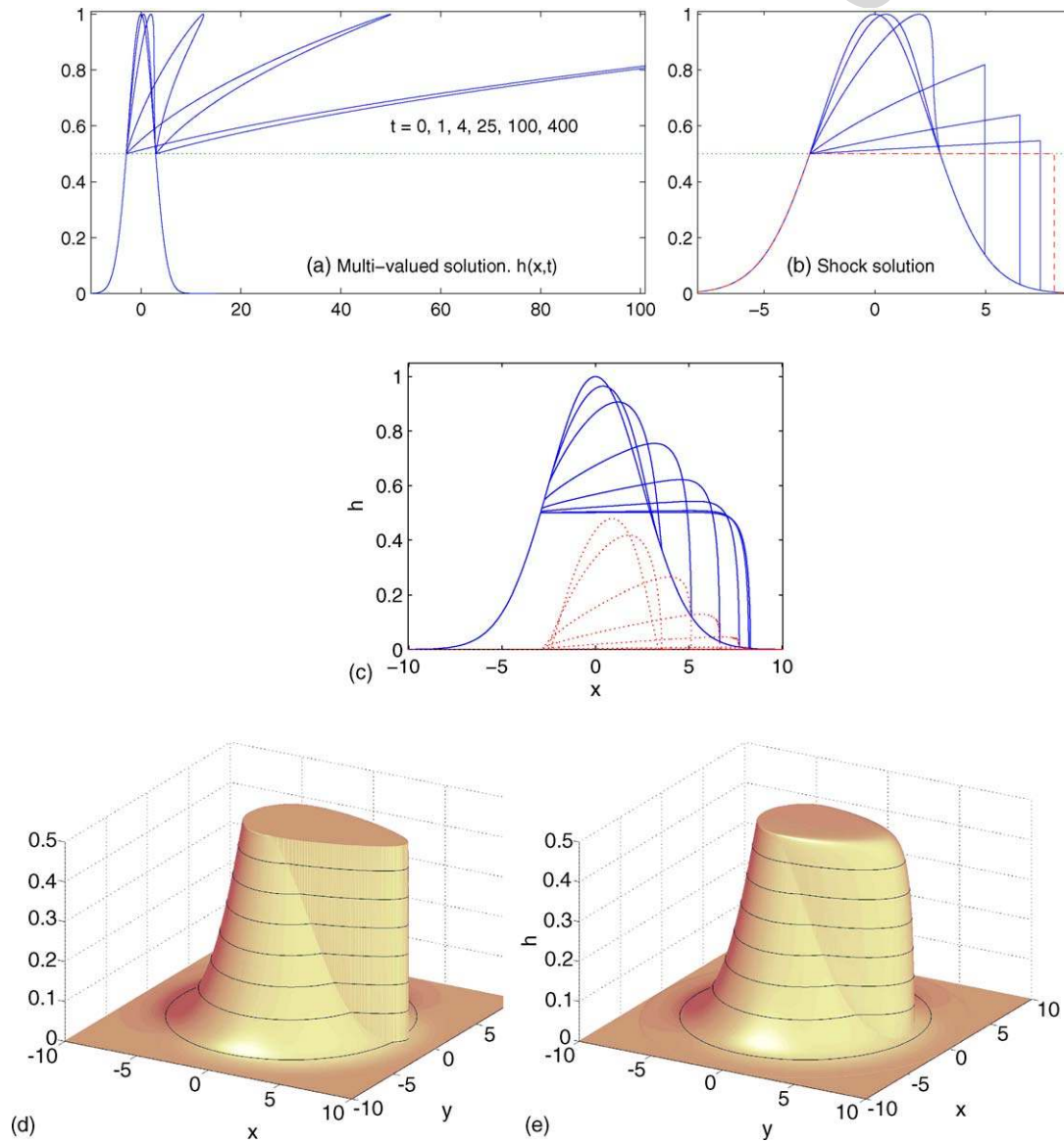


Fig. 3. Slump of Gaussian structures on steep inclined planes. Panels (a) and (b) show the “ $S \gg 1$ ” characteristics solution of the two-dimensional problem with  $h_l = \exp(-2x^2/25)$  and  $B=0.5$ . Shown are snapshots of  $h(x, t)$  at the instants indicated, with and without the shock; the dashed curve is the expected final shape and the dotted line shows  $h=B$ . Panel (c) shows the solution computed numerically using the thin-layer model (the snapshots are at  $t=0, 1, 4, 25, 100, 400, 2500, 10^4$ ;  $Y$  is also included). Panels (d) and (e) show the final shape of a three-dimensional, slumped Gaussian,  $h_l = \exp[-2(x^2 + y^2)/25]$ , as predicted by the “ $S \gg 1$ ” characteristics solution and by direct computation using the ADI scheme, respectively.

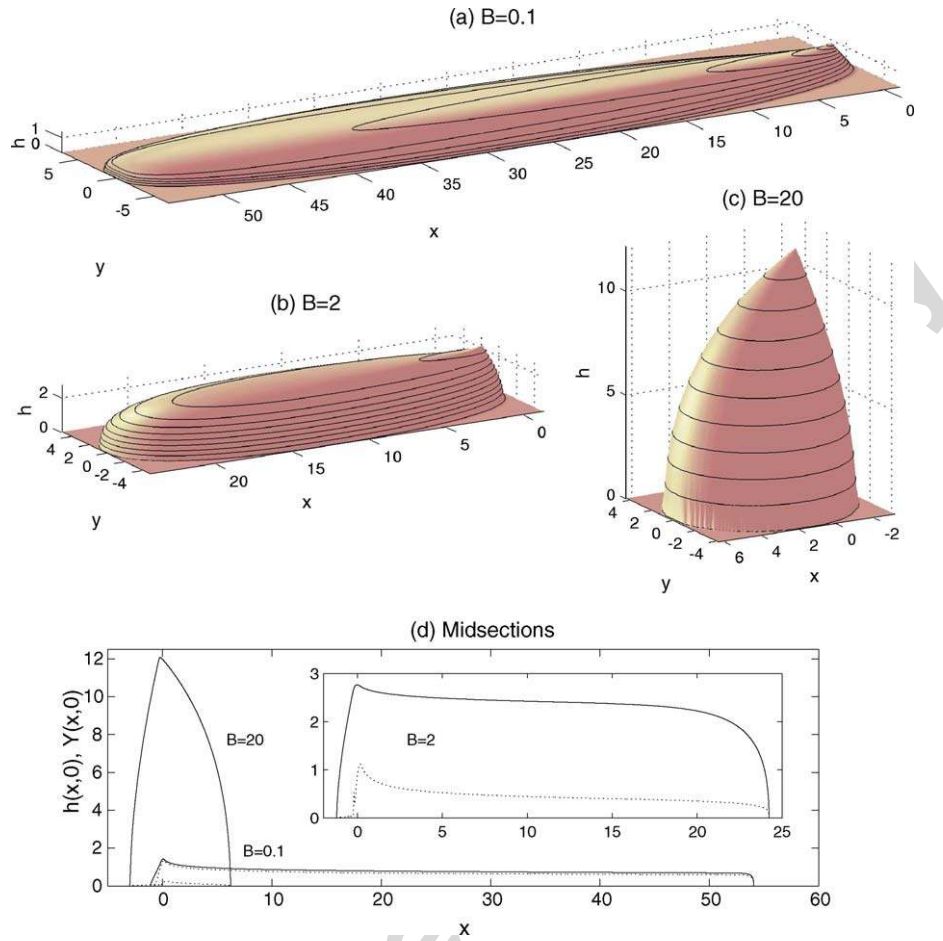


Fig. 4. Dome shapes of extruded domes at  $t=400$  for (a)  $B=0.1$ , (b)  $B=2$  and (c)  $B=20$ . The profiles of  $h$  (solid lines) and  $Y$  (dotted lines) along the midsection of the domes are shown in panel (d).

structure extends over a much larger distance than the vent, the detailed shape of the source becomes unimportant. Note that the centre of the vent is now the origin of our coordinate system.

Figs. 4 and 5 show results for constant-flux extrusions ( $W=1$ ) at three different Bingham numbers:  $B=0.1$ , 2 and 20. The first figure displays the dome shapes after a time  $t=400$ ; the second figure shows a sequence of four snapshots of the domes' edges, together with the (depth-integrated) velocity vectors at  $t=400$ . The low  $B$  extrusion makes little progress up the incline and flows rapidly downslope. Overall, this extrusion is similar to a Newtonian extrusion. Indeed, it is clear from the corresponding  $Y$ -surface (Fig. 4(d)) that the pseudo-plug occupies only a thin superficial layer and most of the fluid is strongly sheared. The large- $B$  case, on the other hand, expands in all directions throughout the period shown; the internal strength of the material is able to withstand the gravitational force down the slope, and the dynamics is dominated by the yield stress (the pseudo-plug occupies almost the whole layer). The intermediate case, with  $B=2$ , lies between the two extremes.

#### 4.1. Similarity scalings

Convenient diagnostics of the extrusion are offered by the furthest positions of the upstream and downstream edges,

$X_{\min}(t)$  and  $X_{\max}(t)$  (respectively), and the maximum half-width,  $Y_{\max}(t)$ . In certain limits of the problem, these diagnostics follow power laws in time that can be deduced from scaling theory.

Conservation of mass demands that the total amount of material extruded at time  $t$  is given by

$$\int_{X_{\min}}^{X_{\max}} \int_{-Y_{\max}}^{Y_{\max}} h(x, y, t) dx dy \equiv \int_0^t W(t) dt, \quad (27)$$

which equals  $t^\alpha$  if we adopt the power-law form,  $W = \alpha t^{\alpha-1}$  (any other pre-factor can be scaled away by suitably choosing the lengthscale  $H$ ).

We now introduce the similarity form,  $h(x, y, t) \sim t^\Delta \phi(\xi, \eta)$ , where  $\xi = xt^{-\gamma}$  and  $\eta = yt^{-\delta}$ . The mass conservation constraint (27) demands  $\Delta = \alpha - \gamma - \delta$ , and the lubrication model becomes

$$\Delta \phi - \xi \gamma \phi_\xi - \eta \delta \phi_\eta + v_\xi + v_\eta = 0, \quad (28)$$

where

$$\begin{pmatrix} v \\ v \end{pmatrix} = \frac{1}{6} t^{2\Delta+1-\gamma} \mathcal{R}^2 (3\phi - \gamma) \begin{pmatrix} S - t^{\Delta-\gamma} \phi_\xi \\ -t^{\gamma+\Delta-2\delta} \phi_\eta \end{pmatrix}, \quad (29)$$

$$\gamma = \phi - \frac{Bt^{\gamma-2\Delta}}{\varsigma} \equiv t^{-\Delta} Y \quad (30)$$



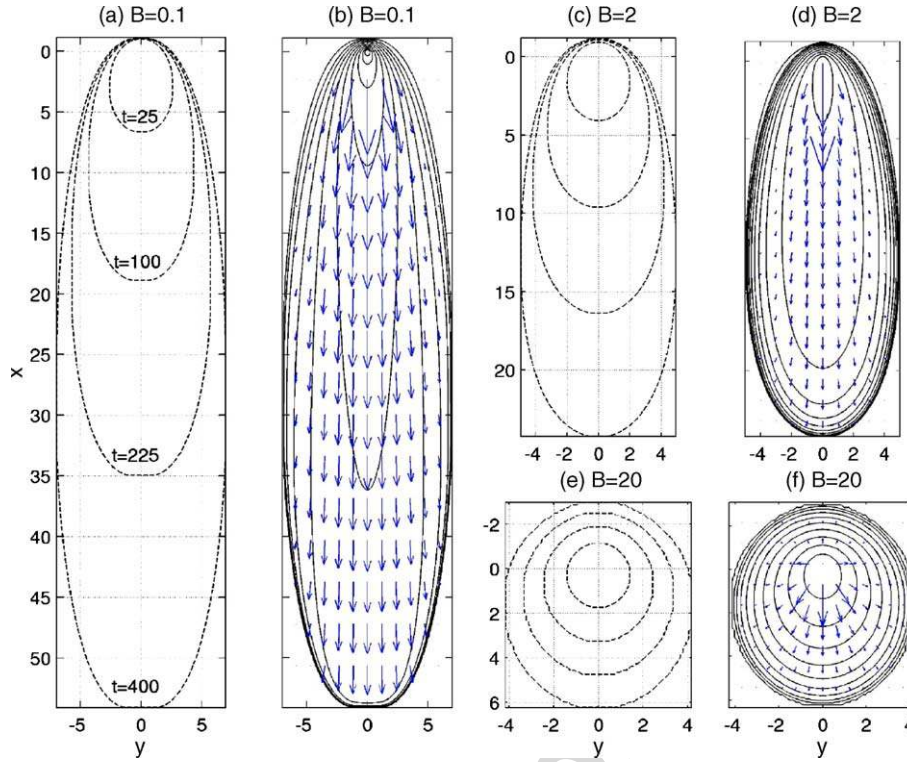


Fig. 5. Panels (a), (c) and (e): a sequence of four snapshots of the edges of the extruded material at times  $t=25$ , 100, 225 and 400. Panels (b), (d) and (f): the depth integrated velocity vectors at  $t=400$  together with contours of constant height. Panels (a) and (b) corresponds to  $B=0.1$ , (c) and (d) to  $B=2$ , and (e) and (f) to  $B=20$ .

and

$$\zeta = \sqrt{(\varphi_\xi - t^{\gamma-\Delta} S)^2 + t^{2(\gamma-\delta)} \varphi_\eta^2} \equiv t^{\gamma-\Delta} s. \quad (31)$$

As described by Balmforth, Craster and Sassi, it is not necessary to solve this equation to determine the characteristic scalings of the dome diagnostics: the time coordinate is embedded within the equation as a parameter and as  $t$  varies, different terms within (29)–(31) grow or decay to enter the dominant balances. Thus, by judicious juggling of the terms, we may deduce the temporal scalings. Moreover, by observing when the dominant balances change, we may estimate when the transitions occur between the different regimes. Note that Balmforth, Craster and Sassi consider only the constant flux case; the current discussion generalizes the results to arbitrary power-law extrusion rates (*i.e.* variable  $\alpha$ ).

The balancing act leads to the following conclusions (for  $\alpha > 0$ ). First, yield stresses and slope play little role in the initial phase of evolution; extrusions begin their life evolving in an axisymmetric Newtonian fashion (cf. [16]). This early life can be curtailed in two different ways: If  $B \gg S$ , the yield stress term becomes large in  $\Upsilon$ , and triggers a transition to a yield-stress dominated state. Expansion continues axisymmetrically for a while, but the downslope component of gravity becomes important at larger times, and there is a second transition to an inclined, yield-stress-dominated state (this final phase does not follow readily from the scaling theory, but can be extracted using an asymptotic expansion designed to construct yield-

stress-dominated domes—see [24]). If  $S \gg B$ , on the other hand, the slope term,  $S$ , emerges in  $s$  and triggers a transition to a slope-dominated, Newtonian state. This state is again a transient because the yield stress term continues to grow in  $\Upsilon$  and eventually triggers another late-time transition to the same final state as before.

We summarize the various scalings and transitions in Fig. 6, and Fig. 7 compares these predictions with the results of numerical simulations. The predictions are largely borne out by the computations; indeed the expected transition times appear to be useful estimates of when the scalings change. However, the computations do not reach the ultimate, yield-stress and slope dominated state because none of the cases computed progress far enough. In fact, the final transitions are expected so late that constraints of resolution prohibit reaching them. These constraints also force us into an underhand computational trick to ensure that we adequately resolve the vent and keep the source flux constant over the duration of long extrusions: when the number of grid points covering the vent becomes too few (typically six points in the  $x$  direction) we start rescaling the vent radius,  $r^*$ , with time, continually enlarging the source (see Appendix A). This has the unfortunate consequence that, eventually, the upslope fluid edge approaches the vent, and the computational predictions for  $X_{\min}$  no longer make sense. We have conveniently omitted this part of the time series of  $X_{\min}$  from Fig. 7. Though not particularly satisfactory, we cannot do any better without introducing a much more sophisticated numerical algorithm, and even this trick fails to allow us access to the asymptotic regime.

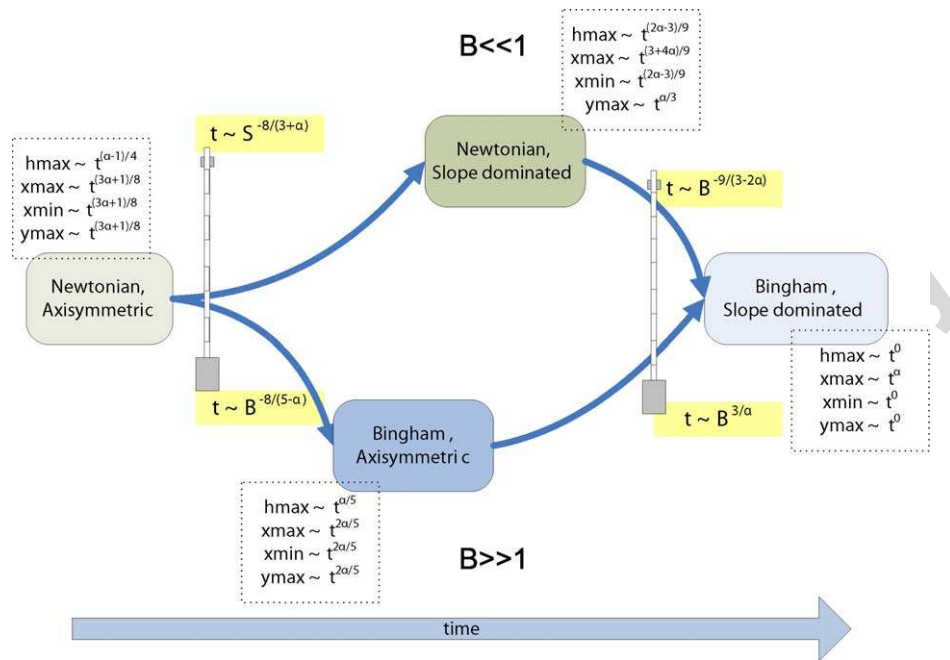


Fig. 6. Scalings and transitions for constant rate extrusions.

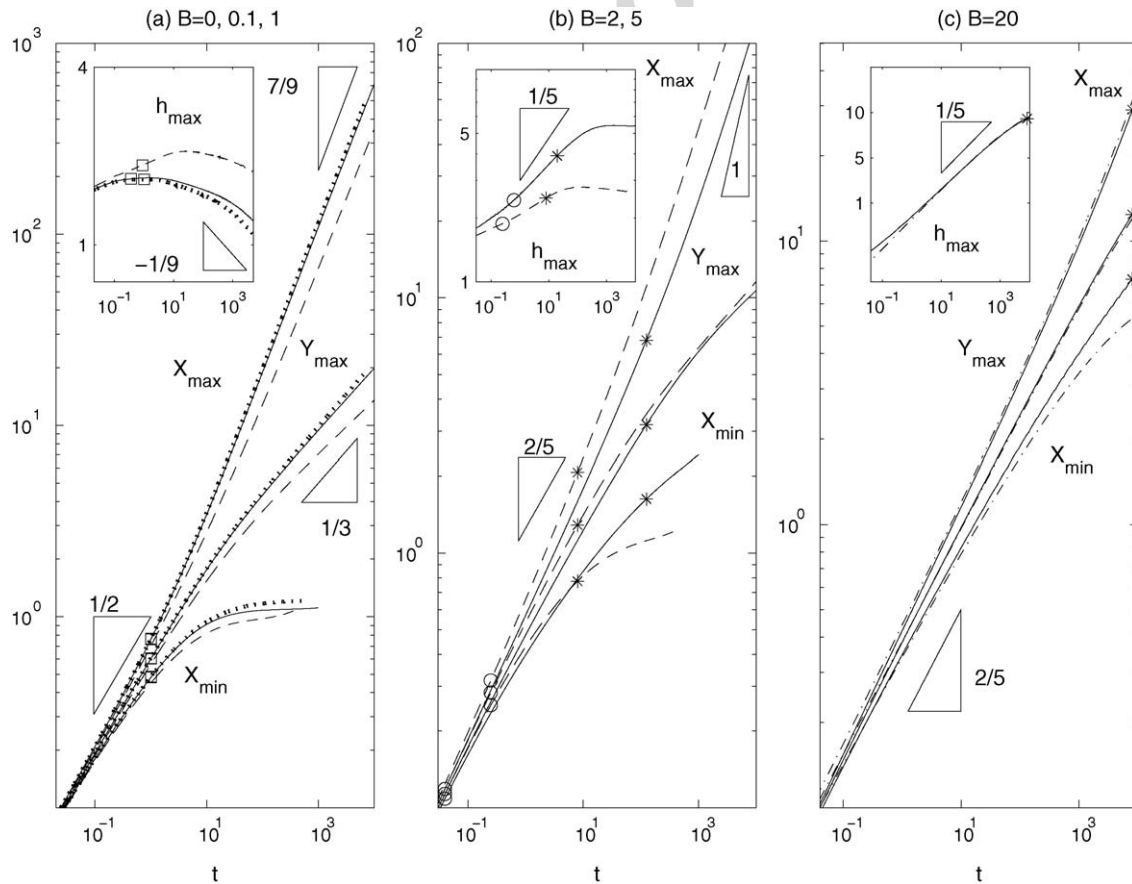


Fig. 7. Evolution of the dome diagnostics for constant-flux extrusions. Panel (a): low Bingham number extrusions with  $B=0$  (dotted),  $B=0.1$  (solid) and  $B=1$  (dashed). The squares denote the expected transition time for when the slope term breaks the axisymmetrical Newtonian scalings ( $t \sim S^{-2} = 1$ ). Panel (b): moderate Bingham number extrusions with  $B=5$  (solid) and  $B=2$  (dashed). The circles show the expected transition time for when the yield stress breaks the axisymmetrical Newtonian scalings ( $t \sim B^{-2}$ ). Panel (c): large Bingham number,  $B=20$  (solid). The dot-dashed line shows the yield-stress dominated asymptotic theory of (24). In panels (c) and (d), the stars indicate the expected transition times for the slope to become important in yield-stress dominated domes ( $t \sim B^3$ ).

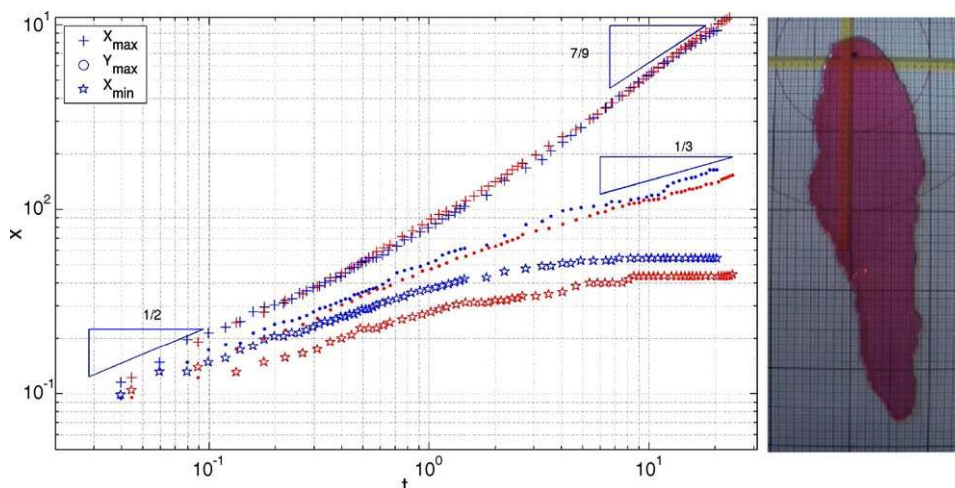


Fig. 8. Experimental extrusions of cornsyrup. Two experiments with slightly different slope are illustrated ( $\tan \phi = 0.046$  and  $0.048$ ), with the dome diagnostics,  $X_{\min}$ ,  $X_{\max}$  and  $Y_{\max}$ , plotted against time. The dimensional measurements are converted into dimensionless values using the slope, viscosity ( $4 \text{ Pa s}$ ), density ( $1.4 \text{ g/cm}^3$ ) and pump rate,  $q$  (equal  $12.2 \text{ cm}^3/\text{min}$ ;  $q = HLV$  and  $H = L \tan \phi$ ). The second picture shows a photograph of one of the extrusions at late times (the syrup is dyed red with food colouring).

#### 4.2. Comparison with experiments

To test the theoretical predictions, we conducted a series of laboratory experiments in which we extruded fluid at constant rate onto an inclined plane. We used two fluids: cornsyrup (as a Newtonian control fluid; density  $1.4 \text{ g/cm}^3$  and viscosity  $4 \text{ Pa s}$ ) and a kaolin slurry (an aqueous suspension of joint compound—a commercially available, kaolin-based building material; density  $1.6 \text{ g/cm}^3$ ).

Extrusions of cornsyrup are presented in Fig. 8, which displays dome diagnostics,  $X_{\min}$ ,  $X_{\max}$  and  $Y_{\max}$ , against time. As predicted by the theory, the dome first expands axisymmetrically, but then slumps downhill; for each phase of evolution, the dependence of the diagnostics on time matches scaling theory. In one sense, this match of theory and experiment is surprising: as illustrated by the photograph included in Fig. 8, the edge of the cornsyrup extrusion becomes much more irregular than the relatively smooth theoretical domes (which are like the low- $B$  example of Fig. 4). We attribute this to surface tension: as the dome grows a capillary ridge develops near the fluid edge, causing incipient, surface-tension-driven fingering of the advancing contact line. The situation is aggravated by the evaporation of water from a superficial “skin”; as evidenced by its ability to buckle and wrinkle, this skin behaves partly elastically and presumably supports some of the stresses exerted on the dome. The surface effects are probably responsible for the qualitative, but not quantitative, agreement between the observed and theoretical dome diagnostics (compare Fig. 8 with the first panel of Fig. 7); Lister [16] presents a better comparison for a different set of experiments.

Kaolin extrusions are shown in Figs. 9 and 10. Measurements made in a cone-and-plate rheometer suggest that this particular material can be fit by a Herschel–Bulkley model with power-law index,  $n \approx 0.5$ , and consistency,  $K \approx 40 \text{ m.k.s.}$  (although no reliable yield stress could be recorded because of wall slip effects).

With such a value for  $n$ , the early time axisymmetric scaling for the dome radius is about  $0.46$ . Fig. 9 shows data from an extrusion onto a flat plane, and presents evidence for a cross-over from this type of scaling to a late-time yield-stress dominated regime in which the scaling of radius falls to  $2/5$ . Also shown in the figure are the results of a theoretical computation in which parameters have been matched to the experiments; except for the earliest times, the observations and theory show quantitative agreement. It is plausible that the discrepancy at early times occurs because the experimental extrusions begin with a finger of unyielded fluid being pushed up through the vent. The finger subsequently fails by collapsing to one side, and the resulting non-axisymmetry obscures the radius scalings at the earliest times.

Fig. 10 shows kaolin extrusions on an inclined plane. Again, there is some evidence for a cross-over from the axisymmetric scalings to the yield-stress dominated ones (particularly in  $Y_{\max}$ ). However, the domes also begin slumping downhill, and the three diagnostics quickly diverge from one another. Fig. 10 again includes theoretical computations with matched parameter settings. The general trends of the observations are reproduced by the theory, although the comparison is not as satisfying as in Fig. 9. We are not completely certain why this should be so, although the rheological parameters are not particularly well constrained by our measurements. The final panel of the figure also presents evidence for an intermediate scaling with  $(X_{\max}, X_{\min}, Y_{\max}) \sim (t^{2/3}, t^0, t^{1/3})$ , which is not expected from the scaling theory (and could merely be an artifact of fitting a power law over too short an interval).

Although the extrusions of the kaolin slurry proceed much more symmetrically and smoothly than those of the syrup, the edges and surface of the kaolin domes still develop imperfections. Previous articles by Blake [3], Griffiths and Fink [6] and Osmond and Griffiths [4] present pictures of surface features on kaolin domes which take the form of a network of



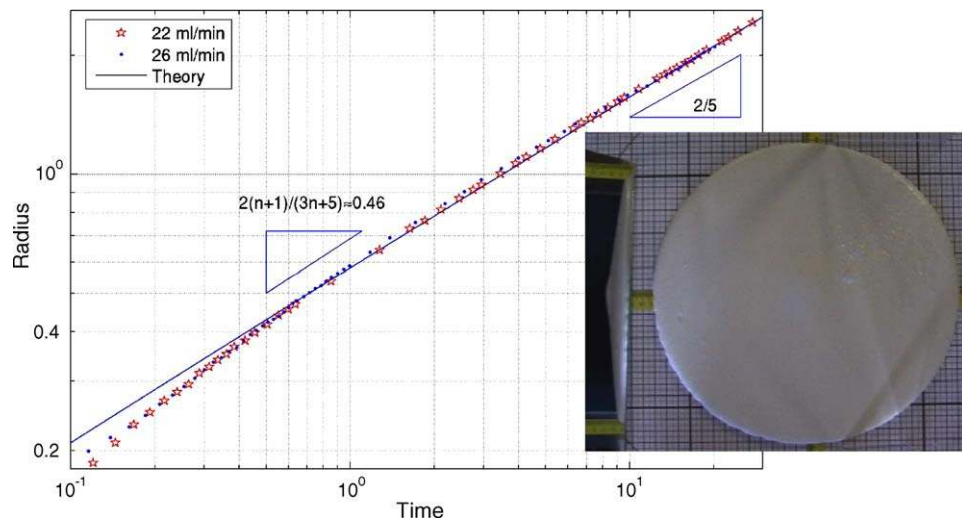


Fig. 9. Experimental extrusions of a kaolin slurry over a horizontal plane. Shown is the average radius (the mean of four measurements in orthogonal directions) against time for two extrusions with different extrusion rates. The dimensional measurements are converted into dimensionless variables by taking  $B = 1$  and using the pumping rate (about 22 and 26  $\text{cm}^3/\text{s}$  for the two experiments),  $K \approx 40 \text{ m.k.s.}$ ,  $n \approx 0.5$ ,  $\rho \approx 1.6 \text{ g/cm}^3$  and  $\tau_y \approx 13 \text{ Pa}$  (as estimated by (47)). The solid curve also included in the picture is the result of a theoretical extrusion, with parameter settings matched to the experimental conditions. The photograph shows a top view of one of the extruded domes at late times; a tilted mirror offers a side view.

intersecting arcs or grooves. Analogous textures formed in all our experiments, and as these grooves became more extensive and prominent, some of our domes also developed small-scale, saw-tooth-like patterns at their edges (see Fig. 11). The edge structure is more pronounced in experiments with longer extru-

sions times and seems to be connected to the drying out of the dome surface. Although the causes of both the surface arcs and edge imperfections remain unknown, the two appear to be related because prominent grooves typically terminate between the “teeth” (e.g. Fig. 11b). Stick-slip or surface ten-

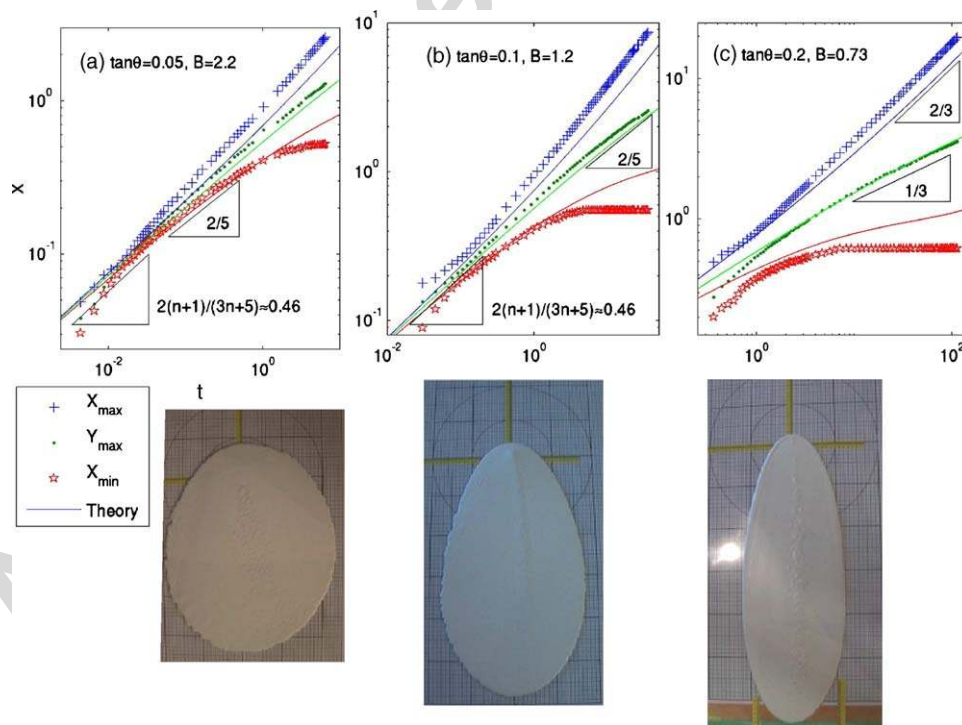


Fig. 10. Experimental extrusions of a kaolin slurry. Panels (a)–(c) show the dome diagnostics,  $X_{\min}$ ,  $X_{\max}$  and  $Y_{\max}$ , against time for three extrusions on planes with varying slope (as indicated). These panels show the dimensionless diagnostics versus dimensionless time; the dimensional measurements are converted into dimensionless variables by taking  $S = 1$  and using the pumping rate (about 13  $\text{cm}^3/\text{min}$ ),  $K \approx 40 \text{ m.k.s.}$ ,  $n \approx 0.5$ ,  $\rho \approx 1.6 \text{ g/cm}^3$  and  $\tau_y \approx 13 \text{ Pa}$  (which also give the values of  $B$  indicated). The solid curves shows the results of theoretical extrusions, with parameter settings matched to the experimental conditions. The three photographs show the extruded domes at times of 6000, 4670 and 3120 sees (dimensionless times of 6.5, 35.4, 114).





Fig. 11. Photographs of surface features on extruded, inclined kaolin domes. The top left photograph shows the network of intersecting curves close to the vent. The top right picture shows the serrated fluid edge and the surface grooves connecting to it. The bottom picture shows what appears to be buckling and folding of the strips carved by the grooves.

sion effects might be responsible, induced by the drying of the fluid edge and surface layers.<sup>2</sup> A change in rheology is further suggested by the buckling and folding of surface strips between the grooves, which occurred later in the same experiments (Fig. 11c).

## 5. Slumps

Our second problem surrounds the release of a finite volume of material, or slump for short.

### 5.1. Axisymmetrical dam breaks

We begin with the circular dam break on a flat surface. In circular polar coordinates, the initial condition can be conveniently written in the form,

$$h(r, 0) = \begin{cases} 1, & r \leq 1, \\ 0, & r > 1. \end{cases} \quad (32)$$

The resulting slumps fall into two categories depending on whether the Bingham number is greater or less than a critical value,  $B_c = (2/15)^{1/2}$ . The two kinds of slumps are illustrated in Fig. 12, and are similar to the edge collapses of planar slumps described in Section 3.1. In either case, the slump begins with the yield and collapse of the fluid edge. For  $B > B_c$ , the internal strength arrests the collapse before the yielded margins of the dome reach the centre, resulting in a partial slump with an inner core of stagnant fluid. For  $B < B_c$ , on the other hand, the internal strength is unable to prevent the entire mound of fluid from yielding, and a complete slump occurs.

The final states are given by

$$B < B_c : h(r, \infty) = \begin{cases} \sqrt{2B(R_\infty - r)}, & 0 \leq r \leq R_\infty, \\ 0, & r > R_\infty \end{cases}, \quad (33)$$

with

$$R_\infty = \left[ \left( \frac{15}{8} \right)^2 \frac{1}{2B} \right]^{1/5} \quad \text{and} \quad h(0, \infty) = \sqrt{2BR_\infty}, \quad (34)$$

or

$$B > B_c : h(r, \infty) = \begin{cases} 1, & r < R_c \\ \sqrt{2B(R_\infty - R)}, & R_c \leq r \leq R_\infty \\ 0, & r > R_\infty \end{cases} \quad (35)$$

where  $R_c$  denotes the inner radius of the yielded regions and

$$R_\infty = \frac{1}{6B} + \frac{1}{B} \left( B^2 - B_c^2 + \frac{1}{9} \right)^{1/2}, \quad R_c = R_\infty - \frac{1}{2B}.$$

In both cases,  $R_\infty$  denotes the final maximal radius. Eq. (33) repeats Nye's solution [33], which was written down originally as a plastic model of a glacier.

Note that for partial slumps, the final profile has a discontinuity in surface slope at  $r = R_c$ . That is, there is a circular "scar" disfiguring the final shape. This feature is equivalent to the points of slope discontinuity seen on one-dimensional flows in Section 3. As we will see below, when we incline the plane, the circular arc of the scar becomes distorted into a more complicated geometrical structure.

The convergence of the slump to its final state can be explored with perturbation theory. Following Matson and Hogg's [31] analysis of planar dam breaks, we set

$$h(r, t) = h_\infty(\mathcal{E}) + \Lambda(t)\Theta(\mathcal{E}), \quad \mathcal{E} = \frac{r - r_c(t)}{r_o(t) - r_c(t)}, \quad (36)$$

where  $r_c(t)$  and  $r_o(t)$  denote the inner and outer radii of the yielded annular regions,  $h_\infty(\mathcal{E})$  prescribes the final shape, and  $\Lambda(t)\Theta(\mathcal{E})$  is the perturbation in separable form. By taking  $\Lambda$ ,

<sup>2</sup> To test the idea that stick-slip might be occurring at the base of the dome, we conducted a number of experiments in which half the plane was covered by sandpaper. In the early stages of the experiment, the two sides of the dome were barely different. Later, however, we saw structures developing on the surface and edge mainly on the half of the dome expanding over the smoother part of the plane. Though a little structure did develop on the sandpaper side, this part of the dome was much smoother. The dome expansion also lost its symmetry about the midline. Thus, there does appear to be some effect of the roughness of the underlying surface, which could reflect the influence of effective slip.

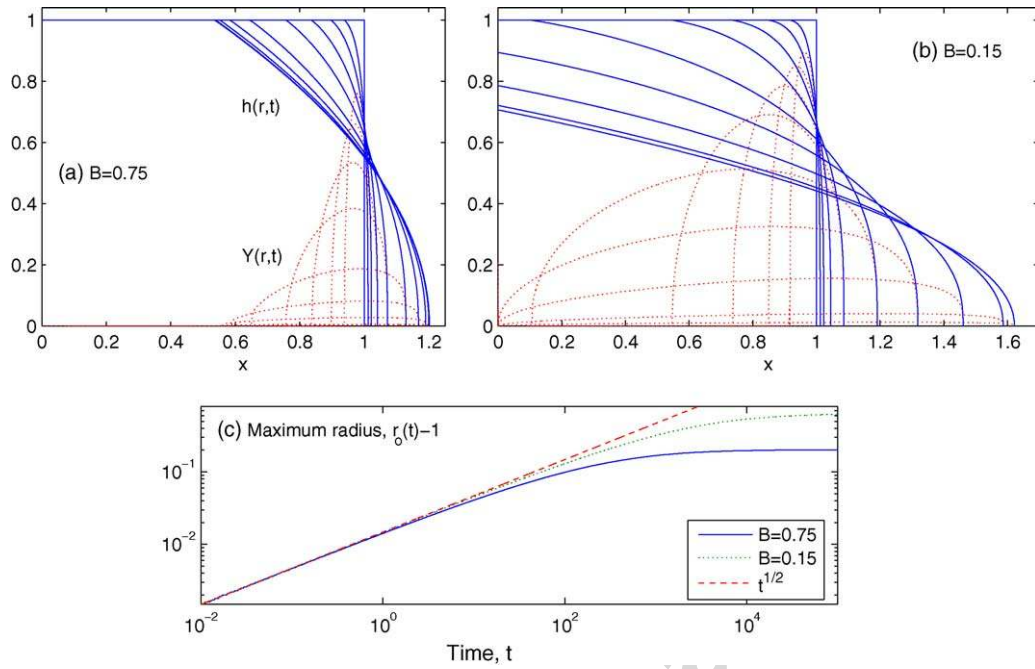


Fig. 12. Axisymmetric dam breaks with initial condition,  $h(r, 0) = 1$  for  $r < 1$  (dots). Shown are snapshots of  $h(r, t)$  (solid curves) and  $Y(r, t)$  (dashed curves) for (a)  $B = 0.75$  and (b)  $B = 0.15$ , at  $t = 0, 0.625, 2.5, 10, 40, 1000, 4000, 25,000, 10^5$ . The crosses and solid curve shows the final profile as given by (33) and numerical computation, respectively. Panel (c) shows a plot of the maximum radius,  $r_o(t)$ , against time.

$|R_c - r_c|$  and  $|R_\infty - r_o|$  all small, we may eventually show that

$$r_o(t) = R_\infty - \left\{ [R_\infty - r_o(0)]^{-1} + \lambda \left[ \frac{B}{h_\infty(0)} \right]^3 t \right\}^{-1}, \quad (37)$$

where  $\lambda \approx 23.3$  is a separation constant that is the eigenvalue of the nonlinear ordinary differential equation (ODE),

$$2\lambda(1 - x^2)(1 - Q) = \frac{d}{dx} [(1 - x^2)Q_x^2], \quad (38)$$

with  $Q(0) = 0$  and regular at  $x = 1$ . Thus, the decay to the final state follows the dependence  $t^{-1}$ .

### 5.2. Slumps on slopes

We consider three types of slumps on slopes:

- (i) The circular dam break, with initial condition (32);
- (ii) The slump of an inclined Nye solution, with  $h(0, t)$  given by (33);
- (iii) The three-dimensional block, with  $h = 1$  for  $-1 < x, y < 1$  and zero beyond.

Figs. 13 and 14 show two examples of inclined circular dam breaks. In the case with large  $B$  in the first figure, the initial column suffers an edge collapse; much of the material remains in place and the very top of the dome falls little during the slump (had the yield stress been slightly larger, the dome would have contained a stagnant core). Conversely, the case with lower  $B$  suffers a layer collapse and slumps quickly downslope, leaving a relatively flat final deposit. In either case, a scar develops

demarking the regions that slumped downhill from those that moved uphill.

An inclined Nye solution is shown in Fig. 15. In this example, a fraction of the upslope portion of the initial dome remains below the yield stress and consequently never yields; this is brought out by the diagnostics,  $X_{\min}$  and  $Y_{\max}$ , which remain at or close to their initial values. Another feature of this slump that is nicely brought out by  $X_{\max}$  is that the advance of the downslope edge is significantly delayed beyond  $t = 0$ . This occurs because the initial dome has a relatively steep (but not vertical) edge with  $|h_x| \sim h^{-1} \gg S$ . Hence, the tilting of the fluid edge has little effect, and it is the central regions that collapse first (in other words, the slump cannot be classified as an edge collapse). Another scar divides the yielded and unyielded portions of the final dome.

Finally, the slump of an inclined block is shown in Fig. 16. The steep sides of the initial condition ensures that this structure slumps in all directions; for this value of  $B$ , the block fully yields although once more the yield strength is almost high enough to hold a central core in place. The final shape is disfigured by multiple scars which are related to the divisions between material that slumped in the four directions.

### 5.3. Scaling and stopping times

To apply the scaling theory of Section 4.1 (with  $\alpha = 0$ ) to the slumps above, we must first revise the analysis to take into account the fact that the initial phases of a slump can contain stagnant zones of fixed height bordered by growing margins of yielded fluid. Initial conditions with flat, central regions have this feature (*i.e.* an edge collapse) provided that their initial depth

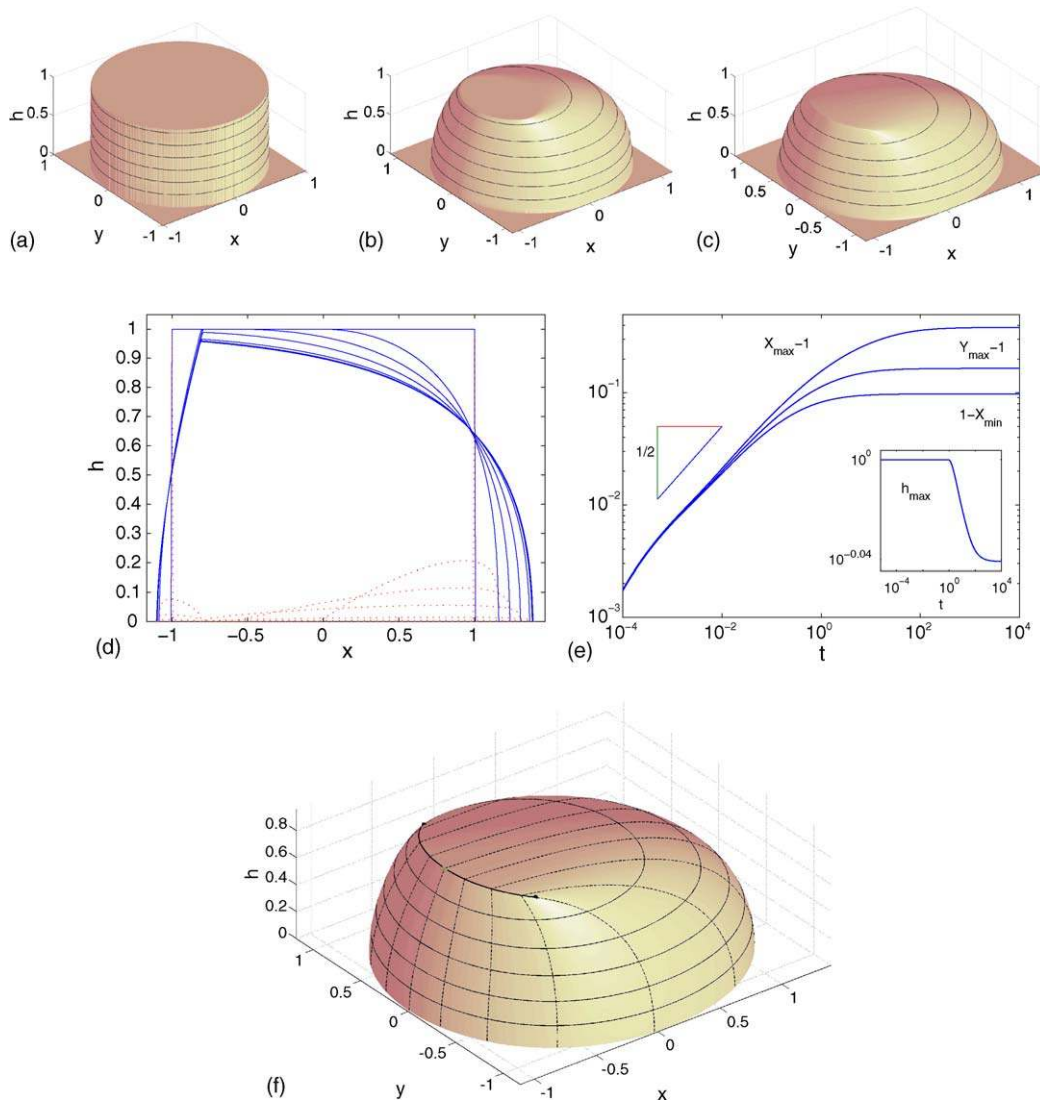


Fig. 13. Circular dam break on an incline for  $B=1$ . The top row of pictures show dome shapes at (a)  $t=0$ , (b)  $t=1$  and (c)  $t=10^4$ . In the middle row, we show snapshots of  $h$  and  $Y$  along the midsection of the dome (for  $t=0, 1, 4, 16, 100, 400, 2500$  and  $10^4$ ), and the evolution of the dome diagnostics. The last picture shows the final shape, as reconstructed from the Charpit solution, and using the footprint of the final dome from the ADI computation. The curve at the top of the dome ended by dots shows the position of the scar. The other lines are contours of constant height and sample characteristic curves.

does not exceed  $B/S$ , or  $B > 1$  with our chosen scalings. In this situation, it does not make sense to apply the mass conservation constraint (27), and we should instead demand that  $\Delta = 0$  (giving fixed height). It follows that slumps begin with a Newtonian phase that is unaffected by either slope or yield stress; the characteristic scalings are  $(X_{\min}, X_{\max}, Y_{\max}) \sim t^{1/2}$ , as seen in the time series of dome diagnostics presented in Figs. 13–16.

As in Section 4.1, this early Newtonian evolution can be interrupted either by the emergence of yield stresses or the slope. However, there is also now a third possibility because the yielding margins of the fluid can at some stage meet, signifying that the whole fluid layer is in motion. At that point, we must reinstate the mass conservation constraint and apply the scaling of Section 4.1 with  $\alpha=0$ . In other words, there can be a transition from partial to complete slump. If the initial structure has a lengthscale ( $\ell$ ), then the time required for the whole layer to yield is  $t \sim \ell^2$ , provided that neither the yield stress nor slope has

broken the early time scalings. Comparing the relative size of  $B$ ,  $S$  and  $\ell$ , we can now categorize the various possible scenarios, which leads us to the scenario shown in Fig. 17.

In brief, if  $B \gg 1$  and  $\ell \gg 1$ , the yield stress dominates first, bringing the partial slump to rest. In this case, we expect a “stopping time”,  $T_{\text{stop}} \sim B^{-2}$ . If the initial structure is sufficiently narrow, on the other hand, and  $\ell^2 \ll B^{-2} \ll 1$ , then even a relatively strong fluid completely slumps after a time,  $t \sim O(\ell^2)$ . The yield stress subsequently brings motion to a halt, giving a stopping time,  $T_{\text{stop}} \sim B^{-8/5}$ .

For  $B \ll 1$ , the yield stress cannot prevent the fluid from fully yielding immediately (*i.e.* there is a layer collapse). Nevertheless, as illustrated in Fig. 14, it still takes time for the structure to lose its original form, and the early time scaling remains as before. For relatively narrow structures,  $\ell \ll 1$ , the slump is first affected by the collapse of the initial structure; only later is there a transition to a slope-dominated Newtonian era. The final

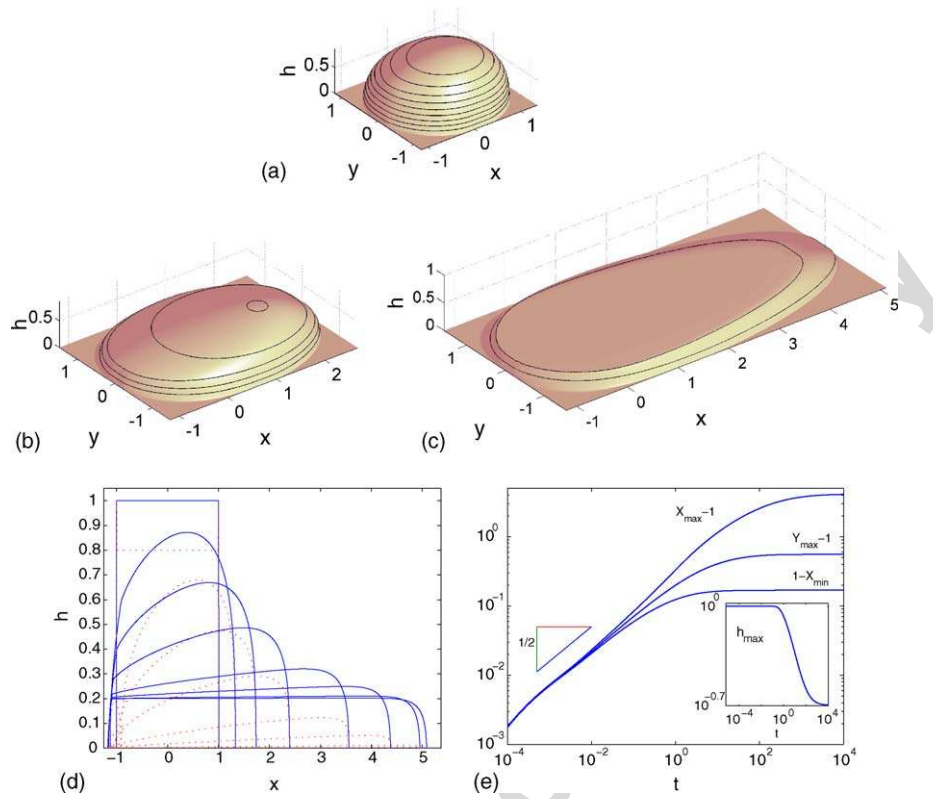


Fig. 14. Circular dam break on an incline for  $B=0.2$ . The top row of pictures show dome shapes at (a)  $t=1$ , (b)  $t=25$  and (c)  $10^4$ . In the middle row, we show snapshots of  $h$  and  $Y$  along the midsection of the dome (for  $t=0, 1, 4, 16, 100, 400, 2500$  and  $10^4$ ), and the evolution of the dome diagnostics.

transition is precipitated by the emergence of the yield stress, giving  $T_{\text{stop}} \sim B^{-3}$ . For  $B \ll 1$  and relatively wide initial conditions,  $\ell \gg 1$ , the slope becomes important first (for  $t \sim O(1)$ ). The ensuing phase of evolution corresponds to the large-slope limit of Section 3.2, which we have not explored in detail.

Fig. 18 presents a summary of numerically determined stopping times for a range of computations. Panel (a) shows results for a flat plane. The numerical data are determined by measuring the length of time required for the edge to reach a given distance of its final position (which is known analytically from formulae in Section 5.1). In particular, we define

$$r_o(T_{\text{stop}}) - r_o(0) = 0.99[R_\infty - r_o(0)], \quad (39)$$

so that the distance travelled by the fluid edge is within one percent of its final value. In this case, scaling theory predicts that  $T_{\text{stop}} \sim B^{-2}$  if  $B \gg 1$ , or  $T_{\text{stop}} \sim B^{-8/5}$  if  $B \ll 1$ , which agree roughly with the numerical data. The figure also includes a more refined estimate of  $T_{\text{stop}}$ , based on the perturbation result in (37):

$$T_{\text{stop}} = \frac{100}{K(R_\infty - 1)} \left[ \frac{h_\infty(0)}{B} \right]^3. \quad (40)$$

The other two panels in Fig. 18 show data for inclined circular dam breaks, with stopping times determined for  $X_{\text{max}}$  and  $Y_{\text{max}}$  in analogy with (39). In these cases, the final values of the dome diagnostics are not known analytically, but they can be extracted from the numerical computations in order to determine  $T_{\text{stop}}$  (more precisely, we take  $X_{\text{max}}(\infty)$  and  $Y_{\text{max}}(\infty)$  to be given by the position of the edge at  $t \sim 10^4$ ). The values of  $B$  over which

the various scalings apparently emerge is, in some cases, quite narrow and the agreement with the predicted slopes is certainly suggestive, but not exact. Panel (b) shows the stopping times for the dam break configuration used above, with an initial radius of unity (*i.e.*  $\ell = 1$ ). In this instance, the large  $B$  data limit to the expected  $B^{-2}$  scaling, but the limiting dependence of  $B^{-3}$  is not reached for the smaller values of  $B$ . To bring out that second scaling, we computed a further suite of dam breaks in which the initial radius was  $1/8$ . As shown in panel (c) of Fig. 18, this second set of data display the expected, low- $B$  behaviour (at least for  $X_{\text{max}}$ ; the other diagnostic comes to rest earlier, which is also clear from the scaling theory). In both cases, we also observe the intermediate scaling,  $T_{\text{stop}} \sim B^{-8/5}$ . Rather curiously, this scaling is observed for  $B < 1$ , whereas theory predicts it should arise only for  $1 \gg B \gg \ell^{-1}$ ; we have no explanation for this, other than a fortuitous coincidence of order one factors.

#### 5.4. Scars

As a slump comes to rest, the fake yield surface  $Y$  approaches the base of the fluid and the pseudo-plug fills the dome. As mentioned in Section 3.1, we then obtain a first-order partial differential equation (PDE) for the shape of the deposit:

$$(S - h_x)^2 + h_y^2 - \frac{B^2}{h^2} = 0. \quad (41)$$

This equation can be solved by Charpit's method (*e.g.* [34]); Balmforth, Craster and Sassi [24] have offered several suggestions on the practicalities. Here, we will follow suit but focus



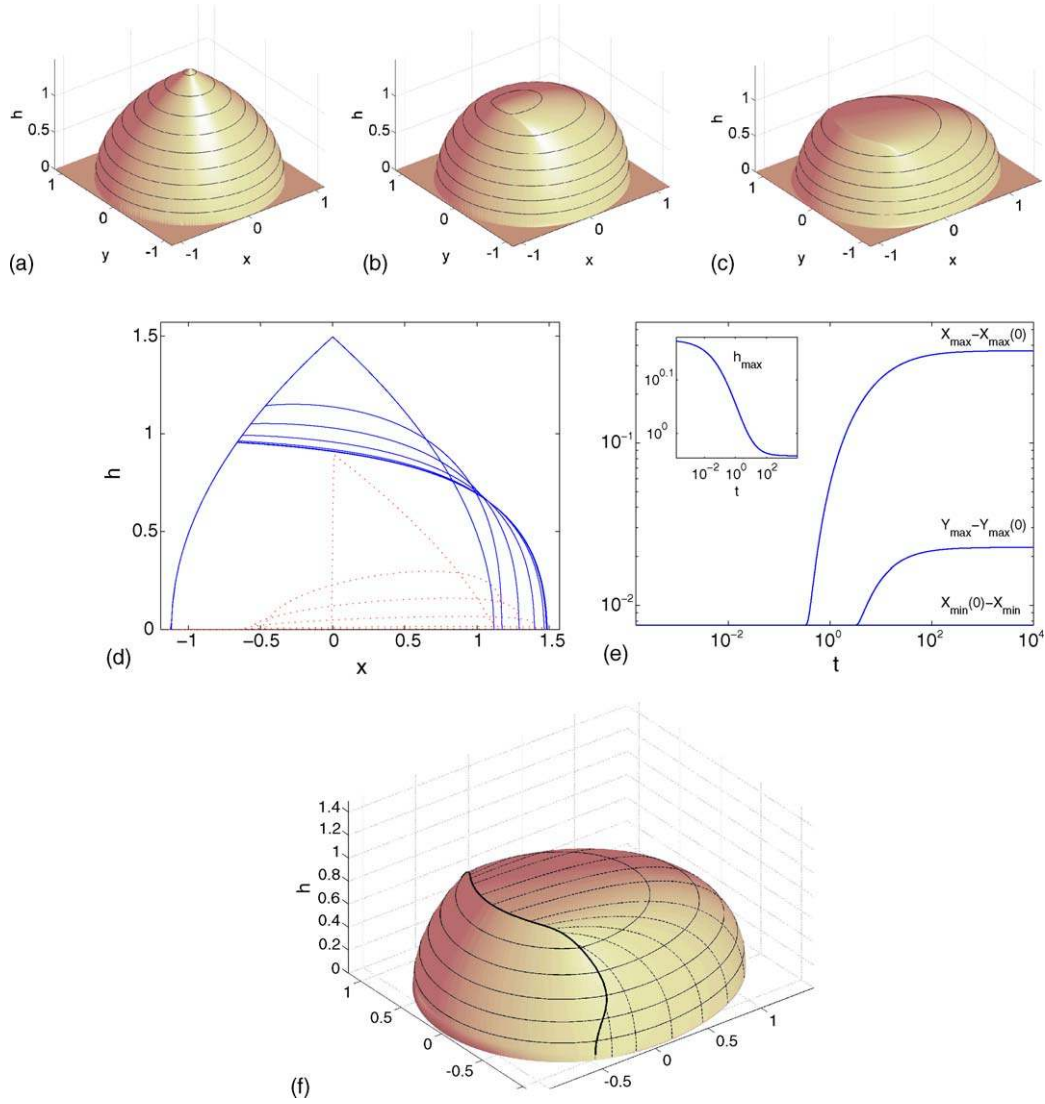


Fig. 15. Collapse of a Nye solution on an incline for  $B=1$  and volume  $\pi$ . The top row of pictures show dome shapes at  $t=0, 1$  and  $10^4$ . In the middle row, we show snapshots of  $h$  and  $Y$  along the midsection of the dome (for  $t=0, 1, 4, 16, 100, 400, 2500$  and  $10^4$ ), and the evolution of the dome diagnostics. The last picture shows the final shape, as reconstructed from the Charpit solution, and using the footprint of the final dome from the ADI computation, but only where the material slumped. The characteristics from the yielded footprint are terminated when they intersect the back of initial dome. In this way, the yielded Charpit solution can be patched onto the unyielded initial dome. The curve cutting through the dome shows the position of the scar that divides yielded from stagnant fluid. The other lines are contours of constant height and sample characteristic curves.

mainly on the case in which one wants to reconstruct  $h$  given the footprint contour on the  $x$ - $y$  plane.

Instead of directly solving for a surface,  $z=h(x, y)$ , the idea behind Charpit's method is to parameterize the solution in terms of two new coordinates, denoted here by  $\zeta$  and  $\kappa$ . The "net" formed by the curves of constant  $\zeta$  and  $\kappa$  can be constructed by setting  $h_x=P(\zeta, \kappa)$  and  $h_y=Q(\zeta, \kappa)$ , and then demanding that  $x, y, h, P$  and  $Q$  solve the ordinary differential equations (ODEs),

$$\begin{aligned} x_\zeta &= F_P = 2(S - P), & y_\zeta &= F_Q = -2Q, \\ h_\zeta &= PF_P + QF_Q = 2P(S - P) - 2Q^2, \\ P_\zeta &= -F_x - PF_h = \frac{2PB^2}{h^3}, & Q_\zeta &= -F_y - QF_h = \frac{2QB^2}{h^3}, \end{aligned} \quad (42)$$

where the PDE is represented by

$$F(x, y, h, P, Q) = \frac{B^2}{h^2} - (S - P)^2 - Q^2 = 0. \quad (43)$$

Finally, we impose the initial condition that for  $\zeta=0$  the curves pass through a point of the footprint contour. Each such *characteristic curve* is indexed by  $\kappa$

From the last two equations in (42), it emerges that  $P_\zeta/P = Q_\zeta/Q$  and so  $P = aQ$ . The value of the parameter  $a = a(\kappa)$  is a property of each characteristic curve, and is fixed once one decides on a parameterization of the footprint contour. Solving Eq. (41) for  $Q$ , and then integrating  $h_\zeta/x_\zeta$  and  $h_\zeta/y_\zeta$ , as obtained from the first three equations in (42), we find

$$x(\kappa, \zeta) - x_0(\kappa) = \frac{h}{S} - \frac{B}{2S^2} \log \left[ \frac{\Delta(h)}{\Delta(0)} \right], \quad (44)$$

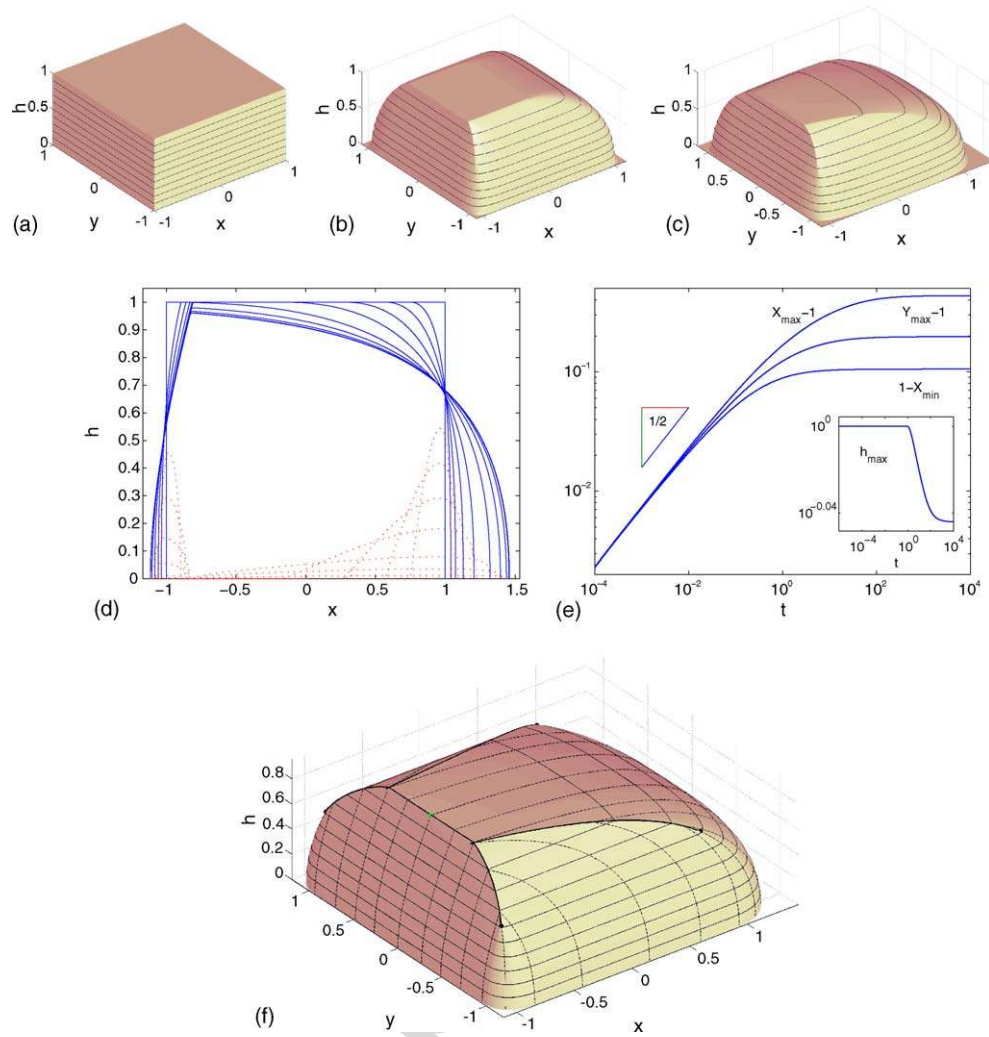


Fig. 16. Collapse of a block on an incline for  $B = 1$ . The top row of pictures show dome shapes at  $t = 0, 1$  and  $10^4$ . In the middle row, we show snapshots of  $h$  and  $Y$  along the midsection of the dome (for  $t = 0, 0.0625, 0.25, 1, 4, 25, 100, 400, 2500$  and  $10^4$ ), and the evolution of the dome diagnostics. The last picture shows the final shape, as reconstructed from the Charpit solution, and using the footprint of the final dome from the ADI computation. The curves ended by dots show the position of the scars. The other lines are contours of constant height and sample characteristic curves.

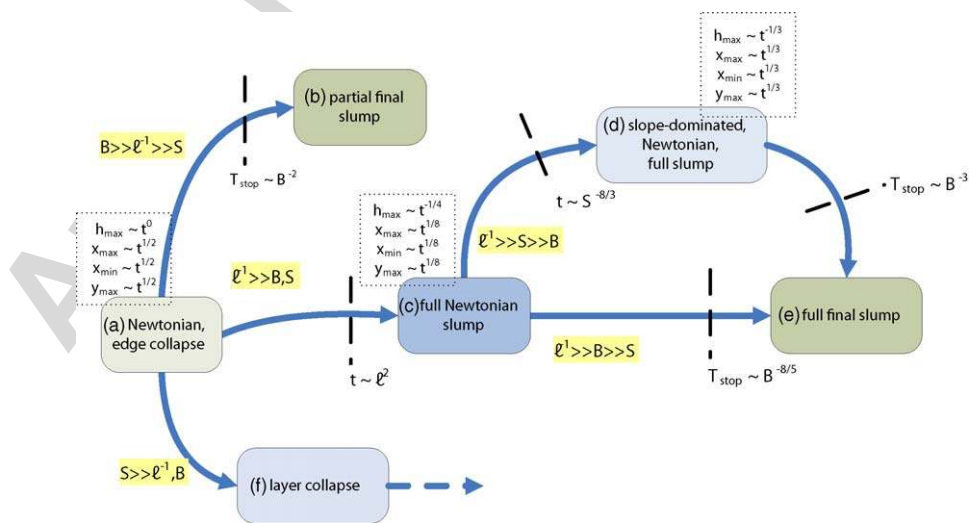


Fig. 17. Scalings and transitions for slumps.

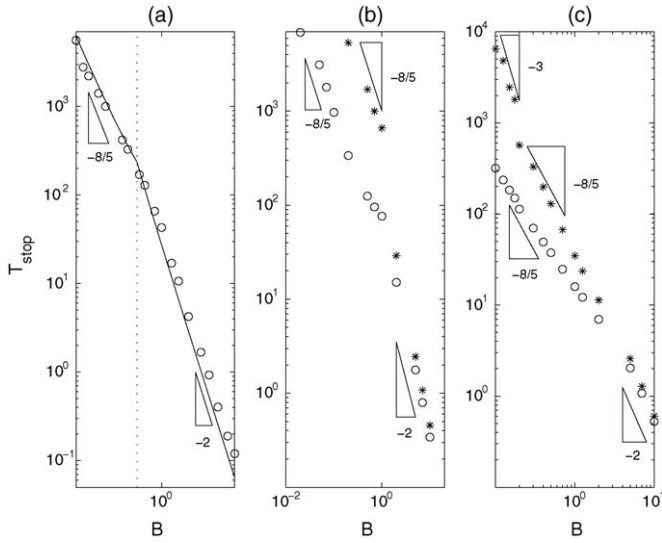


Fig. 18. Panel (a) shows the stopping times for  $X_{\max}$  in the absence of the downslope terms, i.e. the axisymmetric case; the dotted line shows  $B_c$ . Panel (b) shows the stopping times for  $Y_{\max}$  (circles) and  $X_{\max}$  (stars) together with the predictions  $B^{-8/5}$  and  $B^{-2}$ . Panel (c) gives stopping times for a different initial condition:  $h = 1$  for  $r < 1/8$ .

$$y(\kappa, \zeta) - y_0(\kappa) = \frac{1}{S^2} \sqrt{B^2 + a^2(\kappa)B^2 - S^2h^2} - \frac{B}{S^2} \sqrt{1 + a^2(\kappa)}, \quad (45)$$

where

$$\Delta(h) = \left( \frac{aB + \sqrt{B^2 + a^2B^2 - S^2h^2}}{aB - \sqrt{B^2 + a^2B^2 - S^2h^2}} \right) \left( \frac{B + Sh}{B - Sh} \right). \quad (46)$$

These relations provide the solution in  $y \geq 0$ . The solution for  $y < 0$  is obtained with an additional minus sign on the left of (45), and the solution is then symmetric with respect to  $y = 0$  only if the footprint has that symmetry. Note that one can formally take the limit  $S \rightarrow 0$  of (44) and (45), to arrive at the results for a flat plane.

The Eqs. (44) and (45) implicitly determine  $h(x, y)$  given the footprint. Some sample solutions for inclined domes are illustrated in Fig. 19. In these solutions, instead of prescribing the footprint, we instead assume that all the characteristics eventually meet at a single point, which forms the dome's apex and lies at the origin. There we set  $h(0, 0) = 1$ , and (44) and (45) then give the footprint. Balmforth et al. [24] proceed well beyond the construction of such dome shapes and present solutions for the extrusion of yield-stress dominated domes *via* a perturbation theory. The theory also provides the depth-averaged velocity field of the extrusion; Fig. 19 includes such velocity fields. Note that  $B$  must exceed unity; otherwise the dome cannot withstand the pull of gravity and accelerates downslope.

In Fig. 19, the characteristic curves are terminated once they meet at the dome's apex. Though quite natural, this operation is more than a mere convenience: if the curves had been continued any further, the resulting surface would have become multi-valued and unphysical. Thus, terminating the characteristics once they cross is a mathematical necessity. This is also

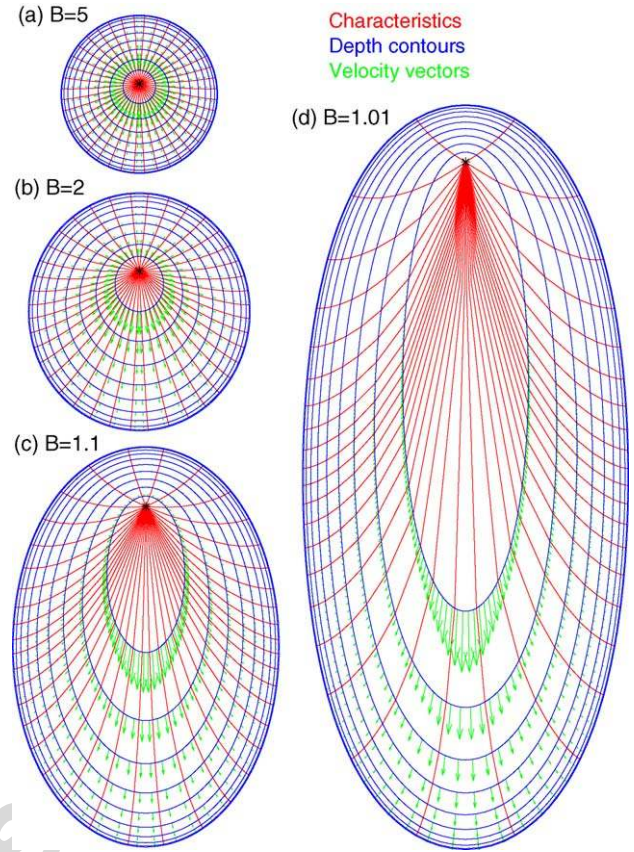


Fig. 19. Charpit solutions for inclined domes. Shown are contours of constant depth (spaced by 0.1), a selection of characteristics, and depth-averaged velocity vectors for four domes with the values of  $B$  indicated. The depth-averaged velocity field is that which would be obtained if the dome were being extruded slowly, and is constructed according to the perturbation theory outlined by Balmforth et al [24].

true in more general situations than an inclined dome with a single pinnacle. Indeed, once that simple geometry is abandoned, it becomes clear that the crossing of the characteristics and the creation of a multi-valued surface is a pervasive feature of the general problem. Moreover, instead of crossing at a single apex, the characteristics meet along curves. In general, a solution can be rendered single-valued and continuous by interrupting the characteristics at their first crossing points and continuing them no further.<sup>3</sup> Because the characteristics typically reach the crossing points with different surface gradients, the height profile then acquires “seams” or “scars” of discontinuous slope along the curves of intersection.

The final panels of Figs. 13, 15 and 16 all show height profiles reconstructed as described above. For the inclined dam break and blocks in Figs. 13 and 16, the characteristics are started off using the locus of final dome edge from the ADI computation. The reconstruction of the inclined Nye solutions is a little more

<sup>3</sup> It is also possible to insert discontinuous shocks into the profiles to make them single-valued. However, we are searching for static shapes and any such discontinuity would normally force the fluid to flow (as in our dam breaks). We are unable to give a mathematical proof that the current construction is the correct one, but by comparing reconstructed height profiles with numerical simulations we are confident that the assumption is sensible.



complicated because the upstream section of the initial structure does not yield during the slump and therefore cannot be built as a Charpit solution. Instead, we first locate the downstream part of the footprint that did yield and build up characteristics from there. We terminate the characteristics when they intersect the upslope side of the initial condition, thereby patching the Charpit solution onto the unyielded part of the dome.

### 5.5. Another comparison with experiments

A difficulty in comparing theoretical slumps with experimental slumps is that it is not straightforward to set up and release a volume of fluid with a given shape on the inclined plane. Dam breaks in channels work quite well [32] because the fluid is confined between three walls and a single gate that can be suddenly raised. Moreover, when the gate is released, the fluid advances past its original position and any spillage and splashes caused by lifting the obstruction are swept away. The same cannot be said of fluid emplaced on a slope beneath a container, especially when we are ultimately interested in the final shape. Indeed, the slump test is a pretty messy device for relatively fluid materials.

To get around any problems with the release mechanism, we avoided confining fluid inside a container and followed a different route, equivalent to some of the theoretical slumps described above. We first extruded a dome of kaolin slurry on a horizontal surface along the lines of Section 4.2, switched off and allowed the dome to come to rest. This produces a structure which is the experimental equivalent of Nye's solution. Once the axisymmetrical dome was at rest, we then quickly tilted the inclined plane to the desired angle and observed the resulting slump. Before-and-after images of two experiments conducted in this way are shown in Fig. 20. In the second experiment, half of the surface of the initial dome was covered with poppy seeds to help track the fluid motion during the slump.

In Fig. 20, we also compare the final shapes with theoretical reconstructions. The latter are generated by first matching parameter values with the experimental conditions: the depth and radius of the initial axisymmetrical dome provide the length scales,  $H \approx 1.6$  cm and  $L \approx 16$  cm. Nye's solution then indicates that

$$\tau_y = \frac{\rho g H^2}{2L} \approx 13.4 \text{ Pa}, \quad (47)$$

given that  $\rho \approx 1.6 \text{ g/cm}^3$ . This scaling implies that  $B = 0.5$  in both experiments, and  $S = (L/H) \tan \phi \approx 10 \tan \phi$ , or  $S \approx 0.6$  and  $1.7$ . Lastly, we use the ADI scheme to solve the corresponding initial-value problem; the final shape, or its reconstruction using the Charpit solution, can be compared directly with experiment. In Fig. 20, we display the Charpit reconstruction, together with its distinctive scar. For both examples, the footprints of the final dome compare favourably with experiment.

Because the experimental domes are so shallow, observing a discontinuity in surface slope (*i.e.* a scar) is difficult. Moreover, the prominent surface texture of our extruded domes obscures what structure there could be. Thus, we are unable to detect experimental analogues of the theoretical scars. Nevertheless, the surface markers in the second experiment do indicate that

only a down-slope portion of the dome slumps after the plane is tilted. In fact, the markers clearly reveal a set of fissures that open up in the surface skin, all downhill of the expected scar.

## 6. Discussion

Our goal in this article has been to summarize recent efforts in developing theory of viscoplastic flow over inclined surfaces. In the slow and shallow limit, we can make much progress using the lubrication approximation, and the results show quantitative agreement with experiments. More specifically, in addition to formulating a model that is straightforwardly and efficiently solved numerically, we can extract analytically the kinematic wave structures [18,22,1], detailed conditions for initiation and cessation of flow, the characteristic time dependence of extrusions, the limiting shape of slumps, and convergence rates to standstill [31]. We end by describing some simple extensions of the theory presented earlier, some unresolved issues, and the generalizations needed to approach a variety of real applications.

### 6.1. Topography

Although we have considered constant inclines, the analysis can be extended to develop lubrication models for flows over topography [35,25,36]. Instead of aligning our coordinates with an inclined plane, we now orientate  $z$  vertically so the  $(x, y)$ —plane is horizontal. The basal topography is denoted by  $F(x, y)$ , the total height of the free surface above the  $z = 0$  plane is represented by  $h(x, y, t) = F(x, y) + \theta(x, y, t)$ , and  $\theta(x, y, t)$  is fluid depth (the special case of constant slope is recovered by taking  $F(x, y) = -Sx$ ). The lubrication analysis proceeds much as before and furnishes the thin-layer model,

$$\partial_t h + \partial_x \mathcal{U} + \partial_y \mathcal{V} = w_s,$$

$$\begin{pmatrix} \mathcal{U} \\ \mathcal{V} \end{pmatrix} = -\frac{1}{6}(3h - Y - 2F)(Y - F)^2 \begin{pmatrix} h_x \\ h_y \end{pmatrix}, \quad (48)$$

where

$$Y = \max \left( h - \frac{B}{\sqrt{h_x^2 + h_y^2}}, F \right). \quad (49)$$

As above, one can solve these equations numerically with a suitable ADI scheme [25]. Instead of proceeding down that pathway, we comment only on how the final shapes of slumped deposits are affected by topography: these shapes are determined by the condition  $Y \rightarrow 0$ , or

$$(F_x + \theta_x)^2 + (F_y + \theta_y)^2 = \frac{B^2}{\theta^2}. \quad (50)$$

This equation can be attacked with Charpit's method, although the elegant simplification of Section 5.4 that allows for a completely analytical solution relies upon (50) being explicitly a function of  $\theta$  and its derivatives, but not of  $x$  and  $y$ . None the less, one can write out the Charpit equations and solve them



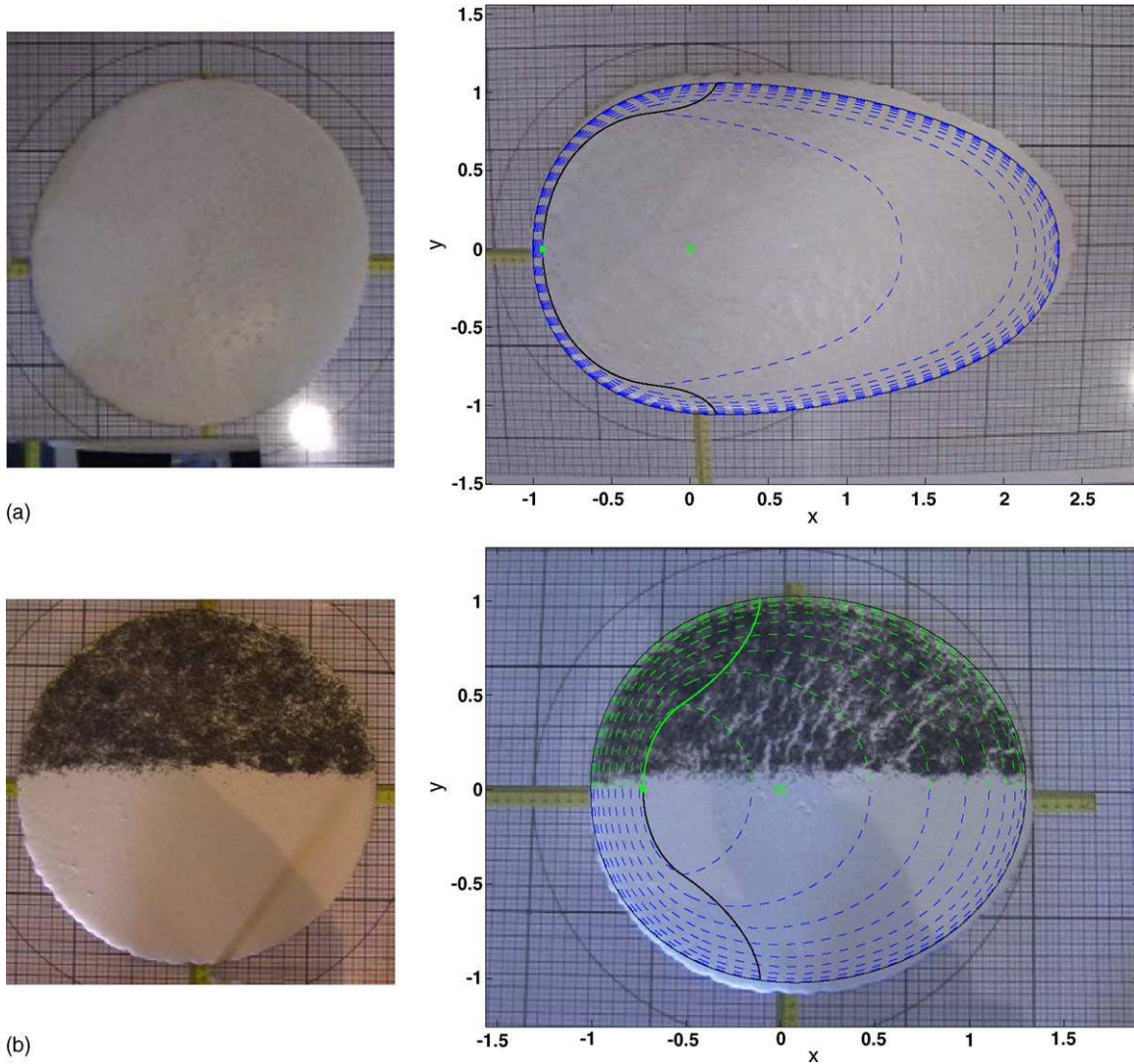


Fig. 20. Photographs of two pump-then-slump experiments. Poppy seeds have been scattered over half the surface of the second experiments by way of surface markers. In the images of the final, slumped domes, contours of constant depth (dotted curves) from theoretical computations are superposed. The circle shows the position of the vent through which the original dome was extruded. The solid curve shows the division between the reconstructed Charpit solution and the unyielded initial dome.

numerically as a system of ODEs. A sample computation for a deposit in a channel ( $F(x, y) = y^2 - x$ ) is shown in Fig. 21.

### 6.2. More complicated constitutive behaviour

Our main discussion has surrounded Herschel–Bulkley fluids, which are analytically convenient but not essential to the derivation of the lubrication model. Indeed, one can try other constitutive laws that build in different material properties. A particularly useful feature of the lubrication analysis is that it simplifies the mathematical structure of complicated constitutive laws and incorporates only the most important physics. One can then tell immediately if a change in the physical model has any impact on a shallow, slow flow, and if it does, the theory offers an expeditious route to finding the consequences. Thus, one could gauge, for example, recent suggestions that thixotropy plays a major role in viscoplastic fluid dynamics [37].

By way of illustration, we consider a generalization of the Herschel–Bulkley model with a slightly more complicated yield condition. Plasticity theory tells us that, in general, a physically sensible constitutive law should have a yield criterion that can be couched as a functional relation between the various invariants of the total stress tensor [1]. In two dimensions, these invariants are the pressure and  $\tau \equiv \sqrt{\tau_{xx}^2 + \tau_{xz}^2}$ , and so the yield criterion must take the general form,  $G(p, \tau) = 0$ , for some function,  $G$ . The von Mises condition embedded in the Herschel–Bulkley law,  $\tau = \tau_y$ , ignores the pressure dependence of the yield condition. By contrast, in theory of granular media, the popular Coulomb law expresses yield in terms of a stress,  $\tau_y = p \tan \psi$ , where  $\psi$  is the internal angle of friction. We combine both examples into the yield condition,

$$\tau = \tau_y(p) \equiv \tau_{0y} + p \tan \psi, \quad (51)$$

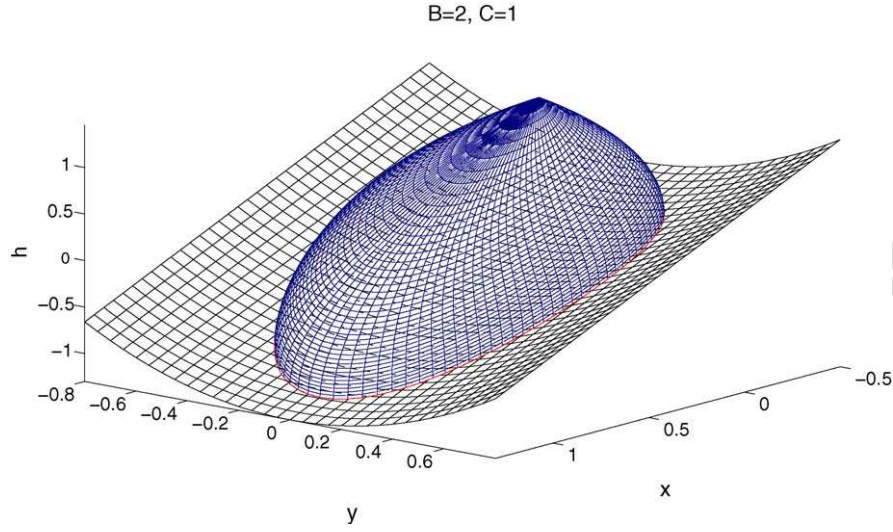


Fig. 21. Height profile of a viscoplastic dome held at its yield stress atop a parabolic channel given by  $F(x, y) = y^2 - x$ .  $B = 2$ .

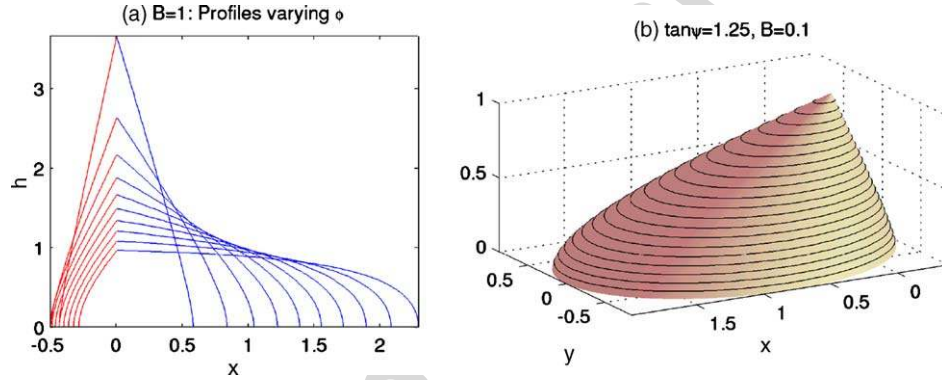


Fig. 22. Limiting shapes with pressure-dependent yield stress. Panel (a) shows height profiles for planar shapes on a slope with  $B = 1$ ; 10 profiles are shown for  $\psi = m\pi/20$ ,  $m = 0, 1, \dots, 9$  (the fluid edges are adjusted so that the profiles have equal area). Panel (b) shows a three-dimensional example with the parameter settings indicated.

where  $\tau_{0y}$  and  $\psi$  are parameters. This model incorporates a pressure dependence into the Herschel–Bulkley law, or allows for cohesion when considered as a model of a granular medium.<sup>4</sup>

In the lubrication analysis, the main impact of the redefinition of  $\tau_y$  is on the shear stress,  $\tau_{xz}$ :

$$\begin{aligned} \tau_{xz} &= (S - h_x)(h - z) \\ &= |u_z|^{n-1} u_z + [B + (h - z)\tan \varphi] \operatorname{sgn}(u_z), \end{aligned} \quad (52)$$

where

$$B = \frac{\tau_{0y} H}{\rho \nu V}, \quad \tan \varphi = \frac{1}{\varepsilon} \tan \psi \quad (53)$$

(unless  $\psi$  is small, the pile of material cannot be shallow). This relation is suitable only provided  $|S - h_x|(h - z) >$

$B + (h - z)\tan \varphi$ , which gives the fake yield surface,

$$Y(x, t) = h - \frac{B}{|S - h_x| - \tan \varphi}. \quad (54)$$

As before, the fluid yields significantly for  $z < Y$ , but only slightly above this surface. Continuing on, we find that the thin-layer equation takes the same form as (16), except for the redefinition of  $Y$ .

Again, we give no complete discussion of the new system, and only explore the consequences on the final shape of a slump: flow ceases when  $Y \rightarrow 0$ , giving the equation for the final profile:

$$h|S - h_x| = B + h \tan \varphi, \quad (55)$$

For  $B = 0$ , this gives  $h = (x - x_0)(S \pm \tan \varphi)$ , where  $x_0$  denotes the position of the fluid edge, and we expect a wedge of “fluid” held at the critical angle,  $\varphi$ , *i.e.* a sandpile. With the cohesion term:

$$h - \frac{B}{(\tan \varphi \pm S)} \log \left[ 1 + h \frac{(\tan \varphi \pm S)}{B} \right] = (S \pm \tan \varphi)(x - x_0).$$

This formula interpolates between our old results and the sandpile. Some sample height profiles are shown in Fig. 22. The sec-

<sup>4</sup> An important difference between Herschel–Bulkley and the Coulomb law is that the former uses the von Mises yield condition, whereas the latter is typically written in terms of Tresca’s condition. The example yield condition in the text is actually equivalent to a Drucker–Prager granular material.

ond solution presented in this figure is obtained from the three-dimensional generalization of (55), namely  $(S - h_x)^2 + h_y^2 = (B + h \tan \varphi)^2 / h^2$ .

### 6.3. Unresolved issues

Although our experiments agree fairly satisfactorily with theory, they expose some thorny issues. In particular, surface textures of various kinds are seen in all the experiments. For corn syrup, we observe a dry, elastic-like skin that can buckle and wrinkle. For kaolin suspensions, the surface becomes grooved with a network of intersecting arcs, and one again sees a distinct skin that may have more plastic-like qualities. Both phenomena motivate an exploration of “elastic/plastic-plated gravity currents” [38], a problem also relevant to fluid films with solidified surfaces (such as lava flows and drying paint). One also wonders whether the features could be used to understand more of the fluid properties, or diagnose the emplacement (flow) conditions given only an image of the final state (often a geological necessity).

The surface grooves on kaolin suspensions, for example, have been likened to slip lines in plasticity theory. Do they also delineate the state of stress in our domes? A difficulty here is that the theory of the slip lines is normally applied to two-dimensional plastic flow, whereas here there are strong shear stresses ( $\tau_{xz}$  and  $\tau_{yz}$ ) acting transverse to the plane of the surface pattern. Nevertheless, the question remains as to what they tell us about the material structure and flow conditions.

### 6.4. Inertial and thick flow

We began our theoretical discussion with two key assumptions, namely that the flow is slow and shallow. Thus, by taking  $\varepsilon \ll 1$  but  $Re$  order one in (9) and (10), we were able to ignore inertial effects. However, relatively fast shallow flows also occur in which the combination  $\varepsilon Re$  can no longer be considered small. Such inertial viscoplastic films have applications in, for example, fast mud flows and landslides. The main problem with adding inertial terms back into the film equations is that we can then no longer integrate the leading-order relations, which remain fully three-dimensional PDEs. Despite this mathematical problem, the allure of the relatively simple thin-film equations has led many researchers to press on regardless and write down inertial generalizations of the lubrication model for Newtonian films. The ideas have also been adapted to viscoplastic fluids [1,39,22]. The reader should be warned that, although these models can be very useful, they are nothing more than uncontrolled approximations (*i.e.* they are not derived from formal asymptotic expansions) of the governing fluid equations; only in the inertialess limit can they be mathematically justified with lubrication theory.

An important practical problem that demands inertial films are roll waves. These are the objects seen on windows and gutters on rainy days. In the viscoplastic context, they have been used to rationalize the surges seen on mud flows [20]. Roll waves on a flowing kaolin suspension in a flume are shown in Fig. 23. As discussed in detail by Balmforth and Liu [40], inertial



Fig. 23. A kaolin suspension flowing down a channel (width 10 cm, flow depth about 0.5 cm) displays the formation of roll waves. Two experiments are shown; in the first, smooth roll waves appear. In the second, the roll waves develop a secondary instability.



generalizations of the viscoplastic film equations can lead to a qualitative description of roll-wave dynamics, but not quantitative one. More specifically, the models are able to rationalize roll waves as the linear instability of the uniform flow and furnish nonlinear structures that resemble them. However, unless one carefully constructs the inertial model via improved averaging techniques [41], the model incorrectly predicts the criterion for the onset of roll waves, and can even generate spurious instabilities.

There are further complications in modelling slow, but not shallow viscoplastic flows: without the thin-layer approximation one must deal with the full Herschel–Bulkley constitutive law, and face all the problems in identifying the yield surfaces. Augmented Lagrangian schemes and regularized constitutive models have become popular in numerical approaches to the problem, as described elsewhere in this volume. However, one also wonders whether insightful analytical progress could be made in some of the limiting situations, such as the approach to rest or the onset of motion. In Section 3.1, we already commented how the limiting shape of a shallow layer could be viewed as a problem of plasticity. Indeed, the fluid need not be shallow for this observation to be made. This poses the question of whether one can construct the limiting shapes of viscoplastic structures using ideas from plasticity theory (such as slip-line theory and Hencky's characteristic net [30]), and without solving the full governing equations as an initial-value problem.

### 6.5. Additional physical effects

In many of the applications of theory of viscoplastic films, other physical effects come into play. Notably, in a variety of problems in geophysics [42,6,43] and nuclear engineering [44,45], the film is non-isothermal and cools as it flows. The changes in temperature can significantly affect the fluid's material properties, or even induce phase changes like the solidification of a surface skin. Attempts to incorporate a thin-layer heat equation and temperature-dependent rheology often run into difficulties in the applications because heat diffusion does not necessarily take place quickly. For example, in lava flows and nuclear coolants, the thermal diffusivity is too low to allow the fluid to become isothermal across its depth. As a result, even though the other fluid equations are simplified by the lubrication approximation, one cannot follow suit with the heat equation and it remains a three dimensional PDE [46,47]. To date, solidification has not been dealt with at all.

Thin films are also often influenced strongly by surface tension. We have ignored this possibility entirely so far, even though it plagues a great many industrial applications and decorates the contact line of a falling film with fingering patterns [48,49]. In this volume, Balmforth et al. [50] incorporate yield stresses into the fingering problem. They derive the generalization of [17] including surface tension, construct steadily propagating planar fronts and test their linear stability to detect fingering instability. But the problem, apart from some experiments [58], remains unexplored.

Finally, we mention slip. Our thin-layer model assumes a no-slip boundary condition on the plane over which the film

flows. However, a large number of complex fluids exhibit the phenomenon of *wall slip*—an effective slip between the fluid and the wall which is usually attributed to the formation of a relatively dilute layer of fluid that lubricates the more concentrated bulk [51]. Much research is still underway to understand and model the phenomenon. Here we mention only that if one trusts a particular parameterization, then it can be incorporated readily into the thin-layer equations (cf. Balmforth et al. [5]). Indeed, one could even turn the problem around, and use thin-layer flows to try to extract a useful parameterization of the slip law. Note that if slip becomes sufficiently severe, the flow can become relatively plug-like across the film thickness. In this circumstance, the shear stresses,  $\tau_{xz}$  and  $\tau_{yz}$ , that normally dominate in the lubrication force balance can be weakened to the point that the extensional stresses,  $(\tau_{xx}, \tau_{yy}, \tau_{zz})$ , and in-plane shear stress,  $\tau_{xy}$ , also enter the problem. The situation, which demands a rather different theoretical model [52], has analogies with theories of free liquid threads and films in fluid mechanics [53], and ice shelves and streams in glaciology [54]. The viscoplastic version of these problems is yet to be addressed.

## Appendix A. Numerical scheme

Our numerical scheme for solving the thin-layer equations is based on the alternating direction implicit (ADI) method [55–57,25]. The main idea is to produce a Crank–Nicholson-like set of equations that deal with each space direction independently, and which still produces a consistent (low order in time) scheme. It is vital to use semi-implicit time-stepping schemes as, after spatial discretization, the governing system of ODEs for the discretized equations is stiff. If one uses central difference approximations for the spatial derivatives then the matrices requiring inversion are tri- or penta-diagonal (cyclic if periodicity is invoked), and sparse inversion routines can be employed. The upshot is that one can construct highly accurate, and reasonably fast, schemes in this manner.

The governing equation for  $h$  is:

$$h_t = \frac{1}{3} \nabla \cdot (C \nabla h) - \frac{S}{3} \partial_x(C), \quad C = \frac{Y^2[3h - Y]}{2}. \quad (\text{A.1})$$

A Crank–Nicholson-style approach is used for the non-linear diffusion terms while the advective piece is treated explicitly. Using the superscript  $(n)$  to denote the  $n$ th time step, one discretises in time to arrive at:

$$\frac{h^{(n+1)} - h^{(n)}}{\Delta t} = \frac{1}{6} \nabla \cdot (C \nabla h)^{(n+1)} + \frac{1}{6} \nabla \cdot (C \nabla h)^{(n)} - \frac{S}{3} \partial_x(C)^{(n)} + O(\Delta t^2) \quad (\text{A.2})$$

To proceed we introduce the two operators

$$\mathcal{L}_x = \left[ I - \frac{\Delta t}{6} \partial_x(C \partial_x) \right], \quad \mathcal{L}_y = \left[ I - \frac{\Delta t}{6} \partial_y(C \partial_y) \right] \quad (\text{A.3})$$

We aim for a first order scheme in time, so  $h_t = [h^{(n+1)} - h^{(n)}] / \Delta t + O(\Delta t)$  with  $h^{(n)}$  as the value of  $h$  at  $t = t_n$ , and  $\Delta t$  as the



time step. The nonlinear terms in  $\mathcal{L}_{x,y}$  are evaluated at  $t=t_n$ . The resulting scheme is then

$$\begin{aligned}\mathcal{L}_x^n \mathcal{H}^{(n)} &= \mathcal{L}_x^{(n)} \mathcal{L}_y^{(n)} [h^{(n+1)} - h^{(n)}] \\ &= \frac{\Delta t}{3} \nabla \cdot (\mathcal{C} \nabla h)^{(n)} - \frac{S \Delta t}{3} \partial_x (\mathcal{C})^{(n)} + O(\Delta t^2).\end{aligned}\quad (\text{A.4})$$

The product of operators,  $\mathcal{L}_x^{(n)} \mathcal{L}_y^{(n)}$  can be inverted sequentially for each direction, and the two-dimensional problem is thereby solved as a pair of one-dimensional ones.

A major issue that we encounter for long-time extrusions is that as the fluid expands, the domain grows continually. We deal with the expanding domain by rescaling the space variables:

$$\xi = \frac{x - M(t)}{L(t)}, \quad \eta = \frac{y}{W(t)} \quad (\text{A.5})$$

where  $L(t)$  is the dome length in the  $x$  direction,  $W(t)$  is half dome width in the  $y$  direction (assuming it to be symmetrical) and  $M(t)$  keeps the dome centered in the computational domain. The change of variables introduces two extra advective terms:

$$h_t \rightarrow h_t - \frac{(\xi \dot{L} + \dot{M}) h_\xi}{L} - \frac{\eta \dot{W} h_\eta}{W}, \quad (\text{A.6})$$

and evolution equations are needed for  $L(t)$ ,  $W(t)$  and  $M(t)$ . The ADI scheme becomes:

$$\begin{aligned}\mathcal{L}_x^{(n)} \mathcal{L}_\eta^{(n)} [h^{(n+1)} - h^{(n)}] &= \frac{\Delta t}{3} \nabla \cdot (\mathcal{C} \nabla h)^{(n)} - \frac{S \Delta t}{3 L^{(n)}} \partial_\xi (\mathcal{C})^{(n)} \\ &\quad + \frac{[\xi(L^{(n+1)} - L^{(n)}) + (M^{(n+1)} - M^{(n)})]}{L^{(n)}} h_{\xi,UP}^{(n)} \\ &\quad + \frac{\eta(W^{(n+1)} - W^{(n)})}{W^{(n)}} h_{\eta,UP}^{(n)},\end{aligned}\quad (\text{A.7})$$

with

$$\mathcal{L}_\xi = \left[ I - \frac{\Delta t}{6 L^2} \partial_\xi (\mathcal{C} \partial_\xi) \right], \quad \mathcal{L}_\eta = \left[ I - \frac{\Delta t}{6 W^2} \partial_\eta (\mathcal{C} \partial_\eta) \right].$$

The rescaling advective terms are computed using a simple first-order upwinding scheme to avoid numerical instability.

The equations for  $L$ ,  $W$  and  $M$  are found by imposing the boundary condition that  $h=0$  at the front (F), back (B) and side (S), and then solving the following equations for  $L^{(n+1)}$ ,  $M^{(n+1)}$  and  $W^{(n+1)}$ :

$$-\text{RHS}^{(n)} = \frac{[\xi(L^{(n+1)} - L^{(n)}) + (M^{(n+1)} - M^{(n)})]}{L^{(n)}} h_\xi^{(n)}$$

at B and F,

$$-\text{RHS}^{(n)} = \frac{\eta(W^{(n+1)} - W^{(n)})}{W^{(n)}} h_\eta^{(n)} \quad \text{at S,}$$

where RHS is the righthand side of (A.7).

## References

[1] C. Ancey, Plasticity and geophysical flows, *J. Non-Newtonian Fluid Mech.* 2006, doi:10.1016/j.jnnfm.2006.05.005.

[2] G. Hulme, The interpretation of lava flow morphology, *Geophys. J. Roy. Astron. Soc.* 39 (1974) 361–383.

[3] S. Blake, Viscoplastic models of lava domes, in: J.H. Fink (Ed.), *Lava Flows and Domes: Emplacement Mechanisms and Hazard Implications*, IAV-CEI Proceedings in Volcanology, vol. 2, Springer-Verlag, 1990, pp. 88–128.

[4] D.I. Osmond, R.W. Griffiths, The static shape of yield-strength fluids slowly emplaced on slopes, *J. Geophys. Res.* 106 (B8) (2001) 16241–16250.

[5] N.J. Balmforth, A.S. Burbidge, R.V. Craster, J. Salzig, A. Shen, Viscoplastic models of isothermal lava domes, *J. Fluid Mech.* 403 (2000) 37–65.

[6] R.W. Griffiths, J.H. Fink, Solidifying Bingham extrusions: a model for the growth of silicic lava domes, *J. Fluid Mech.* 347 (1997) 13–36.

[7] N. Pashias, D.V. Boger, J. Summers, D.J. Glenister, A fifty cent rheometer for yield stress measurement, *J. Rheol.* 40 (1996) 1179–1189.

[8] P. Perona, Bostwick degree and rheological properties: an up-to-date viewpoint, *Appl. Rheol.* 15 (2005) 218–229.

[9] P. Coussot, S. Proust, C. Ancey, Rheological interpretation of deposits of yield stress fluids, *J. Non-Newtonian Fluid Mech.* 66 (1996) 55–70.

[10] J.G. Oldroyd, Rectilinear flow of non-Bingham plastic solids and non-Newtonian viscous liquids II, *Proc. Camb. Phil. Soc.* 47 (1951) 410–418.

[11] I.C. Walton, S.H. Bittleston, The axial flow of a Bingham plastic in a narrow eccentric annulus, *J. Fluid Mech.* 222 (1991) 39–60.

[12] O. Reynolds, On the theory of lubrication and its application to Mr. Beauchamp Tower's experiments, including an experimental determination of the viscosity of olive oil, *Roy. Soc. Philos. Trans. Pt. 1* 177 (1886) 157–234.

[13] H.E. Huppert, The propagation of two-dimensional and axisymmetric viscous gravity currents over a rigid horizontal surface, *J. Fluid Mech.* 121 (1982) 43–58.

[14] H.E. Huppert, Flow and instability of a viscous gravity current down a slope, *Nature* 300 (1982) 427–429.

[15] J.A. Moriarty, L.W. Schwartz, E.O. Tuck, Unsteady spreading of thin liquid films with small surface tension, *Phys. Fluids A* 3 (1991) 733–742.

[16] J.R. Lister, Viscous flows down an inclined plane from point and line sources, *J. Fluid Mech.* 242 (1992) 631–653.

[17] W.S.B. Paterson, *Physics of Glaciers*, 3rd ed., Butterworth-Heinemann, 1999.

[18] K.F. Liu, C.C. Mei, Slow spreading of Bingham fluid on an inclined plane, *J. Fluid Mech.* 207 (1989) 505–529.

[19] K.F. Liu, C.C. Mei, Approximate equations for the slow spreading of a thin sheet of Bingham plastic fluid, *Phys. Fluids A* 2 (1991) 30–36.

[20] C.C. Mei, K.F. Liu, M. Yuh, *Geomorphological fluid mechanics*, Springer Lecture Notes in Physics, Ch. Mud flow - slow and fast (2001) 548–577.

[21] P. Coussot, *Mudflow rheology and dynamics*, IAHR Monograph Series, Balkema, 1997.

[22] X. Huang, M.H. Garcia, A Herschel–Bulkley model for mud flow down a slope, *J. Fluid Mech.* 374 (1998) 305–333.

[23] N.J. Balmforth, R.V. Craster, A consistent thin-layer theory for Bingham fluids, *J. Non-Newtonian Fluid Mech.* 84 (1999) 65–81.

[24] N.J. Balmforth, R.V. Craster, R. Sassi, Shallow viscoplastic flow on an inclined plane, *J. Fluid Mech.* 470 (2002) 1–29.

[25] C.C. Mei, M. Yuh, Slow flow of a Bingham fluid in a shallow channel of finite width, *J. Fluid Mech.* 431 (2001) 135–160.

[26] D. De Kee, R.P. Chabira, M.B. Powley, S. Roy, Flow of viscoplastic fluids on an inclined plane: evaluation of yield stress, *Chem. Eng. Commun.* 96 (1990) 229–239.

[27] P. Coussot, S. Proust, Slow, unconfined spreading of a mudflow, *J. Geophys. Res.* 101 (1996) 25217–25229.

[28] J.A. Chamberlain, J.E. Sader, K.A. Landman, L.R. White, Incipient plane-strain failure of a rectangular block under gravity, *Int. J. Mech. Sci.* 43 (2001) 793–815.

[29] G.G. Lipscomb, M.M. Denn, Flow of Bingham fluids in complex geometries, *J. Non-Newtonian Fluid Mech.* 14 (1984) 337–346.

[30] R. Hill, *The Mathematical Theory of Plasticity*, Oxford University Press, 1950.

[31] G.P. Matson, A.J. Hogg, 2D Bingham gravity currents approach to final state, *J. Non-Newtonian Fluid Mech.* 2006, doi:10.1016/j.jnnfm.2006.05.003.

- [32] N.J. Balmforth, R.V. Craster, P. Perona, A. Rust, R. Sassi, The Bostwick consistometer and viscoplastic dam breaks, *J. Non-Newtonian Fluid Mech.* 2006, doi:10.1016/j.jnnfm.2006.06.005.
- [33] J.F. Nye, The mechanics of glacier flow, *J. Glaciol.* 2 (1952) 82–93.
- [34] I.N. Sneddon, *Elements of Partial Differential Equations*, McGraw-Hill, 1957.
- [35] M. Yui, C.C. Mei, Slow spreading of fluid mud over a conical surface, *J. Fluid Mech.* 519 (2004) 337–358.
- [36] M. Ambrose, Slow flow of visco-plastic material, Master's Thesis, Imperial College London, 2004.
- [37] P. Coussot, Q.D. Nguyen, H.T. Huynh, D. Bonn, Viscosity bifurcation in thixotropic, yielding fluids, *J. Rheol.* 46 (2002) 573–589.
- [38] A. Slim, Elastic-plasted gravity currents, in: S. Ghadge (Ed.), *Proceedings of the Geophysical Fluid Dynamics Summer Program*, Woods Hole Oceanographic Institution, 2004.
- [39] K.F. Liu, C.C. Mei, Roll waves on a layer of a muddy fluid down a gentle slope—a Bingham model, *Phys. Fluids* 6 (1994) 2577–2590.
- [40] N.J. Balmforth, J.J. Liu, Roll waves in mud, *J. Fluid Mech.* 519 (2004) 33–54.
- [41] C. Ruyer-Quil, P. Manneville, Further accuracy and convergence results on the modelling of flows down inclined planes by weighted-residual approximations, *Phys. Fluids* 17 (2002) 170–183.
- [42] R.W. Griffiths, The dynamics of lava flows, *Annu. Rev. Fluid Mech.* 32 (2000) 477–518.
- [43] R.W. Griffiths, R.C. Kerr, K.V. Cashman, Patterns of solidification in channel flows with surface cooling, *J. Fluid Mech.* 496 (2003) 33–62.
- [44] D. Vola, F. Babik, J.C. Latche, On a numerical strategy to compute gravity currents of non-Newtonian fluids, *J. Comp. Phys.* 201 (2004) 397–420.
- [45] T.N. Dinh, M.J. Konovalikhin, B.R. Sehgal, Core melt spreading on a reactor containment floor, *Prog. Nucl. Eng.* 36 (2000) 405–468.
- [46] N.J. Balmforth, R.V. Craster, Dynamics of cooling domes of viscoplastic fluid, *J. Fluid Mech.* 422 (2000) 225–247.
- [47] N.J. Balmforth, R.V. Craster, R. Sassi, Dynamics of cooling viscoplastic domes, *J. Fluid Mech.* 499 (2004) 149–182.
- [48] H.E. Huppert, Flow and instability of a viscous gravity current down a slope, *Nature* 300 (1982) 427–429.
- [49] M.H. Eres, L.W. Schwartz, R.V. Roy, Fingering phenomena for driven coating films, *Phys. Fluids* 12 (2000) 1278–1295.
- [50] N.J. Balmforth, S. Ghadge, T. Myers, Fingering of a viscoplastic contact line, *J. Non-Newtonian Fluid Mech.* 2006, doi:10.1016/j.jnnfm.2006.07.011.
- [51] H.A. Barnes, A review of the slip (wall depletion) of polymer solutions, emulsions and particle suspensions in viscometers: its cause, character, and cure, *J. Non-Newtonian Fluid Mech.* 56 (1995) 221–251.
- [52] N.J. Balmforth, R.V. Craster, C. Toniolo, Interfacial instability in non-newtonian fluid layers, *Phys. Fluids* 15 (2003) 3370–3384.
- [53] A. Oron, S.H. Davis, S.G. Bankoff, Long-scale evolution of thin liquid films, *Rev. Mod. Phys.* 69 (1997) 931–980.
- [54] D.R. MacAyeal, Large-scale ice flow over a viscous basal sediment: theory and applications to ice stream b, Antarctica, *J. Geophys. Res.* 94 (B4) (1987) 4071–4087.
- [55] G.I. Marchuk, Splitting and alternating direction methods, in: P.G. Ciarlet, J.-L. Lions (Eds.), *Handbook of Numerical Analysis*, vol. 1, North-Holland, Amsterdam, 1990, pp. 197–462.
- [56] W.H. Press, B.P. Flannery, S.A. Teukolsky, W.T. Vetterling, *Numerical Recipes: The Art of Scientific Computing*, Cambridge University Press, 1986.
- [57] T.P. Witelski, M. Bowen, ADI schemes for higher-order nonlinear diffusion equations, *Appl. Num. Math.* 45 (2003) 331–351.
- [58] J.R. de Bruyn, P. Haddas, S. Kim, Fingering instability of a sheet of yield-stress fluid, *Phys. Rev. E* 66 (2002) (art no. 031504).
- [59] S.K. Wilson, B.R. Duffy, A.B. Ross, On the gravity-driven draining of a rivulet of a viscoplastic material down a slowly varying substrate, *Phys. Fluids* 14 (2002) 555–571.
- [60] A.B. Ross, S.K. Wilson, B.R. Duffy, Thin-film flow of a viscoplastic material round a large horizontal stationary or rotating cylinder, *J. Fluid Mech.* 430 (2001) 309–333.
- [61] S.D.R. Wilson, S.L. Burgess, The steady, spreading flow of a rivulet of mud, *J. Non-Newtonian Fluid Mech.* 79 (1998) 77–85.
- [62] P.C. Smith, A similarity solution for slow viscous flow down an inclined plane, *J. Fluid Mech.* 58 (1973) 257–288.